Intelligent automatic operational modal analysis

Mechanical Systems and Signal Processing 201 (2023) 110669

Contents lists available at ScienceDirect

Mechanical Systems and Signal Processing

journal homepage: www.elsevier.com/locate/ymssp

Intelligent automatic operational modal analysis

Marco Martino Rosso [a,*], Angelo Aloisio [b], Jafarali Parol [c], Giuseppe Carlo Marano [a], Giuseppe Quaranta [d]

[a] Department of Structural, Geotechnical and Building Engineering, Politecnico di Torino, Corso Duca Degli Abruzzi 24, 10128 Turin, Italy
[b] Civil, Environmental and Architectural Engineering Department, Universita' degli Studi dell'Aquila, Via Giovanni Gronchi 18, 67100 L'Aquila, Italy
[c] Energy and Building Research Center, Kuwait Institute for Scientific Research, Kuwait City, Kuwait
[d] Department of Structural and Geotechnical Engineering, Sapienza University of Rome, Via Eudossiana 18, 00184 Rome, Italy

ARTICLE INFO

Communicated by J.E. Mottershead

Keywords:
Machine learning
Operational modal analysis
Random forest
Stabilization diagram
Stochastic subspace identification
Tall building
Uncertainty propagation

ABSTRACT

Operational modal analysis methods have been proven especially useful to identify existing structures and infrastructures under serviceability conditions. However, the installation of sensing systems for monitoring continuously an ever larger number of existing constructions has motivated significant efforts towards the automation of the available methods.

Within this framework, the present paper introduces a new paradigm for the automatic output-only modal identification of linear structures under ambient vibrations, namely the intelligent automatic operational modal analysis (i-AOMA). It exploits the covariance-based stochastic subspace (SSI-cov) algorithm for the output-only identification of the modal parameters and its workflow consists of two main phases. Initially, quasi-random samples of the control parameters for the SSI-cov algorithm are generated. Once the SSI-cov algorithm is performed for each sample, the corresponding stabilization diagrams are processed in order to prepare a database for training the intelligent core of the i-AOMA method. This is a machine learning technique (namely a random forest algorithm) that predicts which combination of the control parameters for the SSI-cov algorithm is able to provide good modal estimates. Afterward, new quasi-random samples of the control parameters for the SSI-cov algorithm are generated repeatedly until a statistical convergence criterion is achieved. If the generic sample is classified as feasible by the intelligent core of the i-AOMA method, then the SSI-cov algorithm is performed. Finally, stable modal results are distilled from the stabilization diagrams and relevant statistics are computed to evaluate the uncertainty level due to the variability of the control parameters.

The proposed i-AOMA method has been applied to identify the modal features of the Al-Hamra Firduos Tower, an iconic 412.6 m tall building located in Kuwait City (Kuwait). The final results well agree with a previous experimental study, and it was also possible to identify two new vibration modes of the structure. The implemented open-source Python code is made freely available.

1. Introduction

The growing use of structural health monitoring (SHM) requires efficient solutions that aim at automatizing the extraction of the modal parameters (viz., natural frequencies, mode shapes, and damping ratios) from the recorded dynamic response of the structures.

* Corresponding author.
E-mail address: marco.rosso@polito.it (M.M. Rosso).

https://doi.org/10.1016/j.ymssp.2023.110669
Received 7 May 2023; Received in revised form 17 July 2023; Accepted 4 August 2023
Available online 16 August 2023

This need originated the development of some strategies able to facilitate the identification of the modal parameters under free or ambient vibrations, in such a way to mitigate the influence of analyst's decisions on the whole elaboration process [1,2].

Within this framework, the stochastic subspace identification (SSI) algorithm [3,4] is often considered for the automatic operational modal analysis (AOMA) of linear structures subjected to ambient vibrations. Specifically, the automatic identification via SSI algorithm is commonly performed either from the covariances of the outputs (SSI-cov) [5–13] or directly from time series collected at the tested structure by means of projections (SSI-data) [14–19]. Regardless the specific version, the implementation of proper strategies is required to make fully automatic each elaboration phase of the general workflow of the SSI algorithm, namely:

- definition of the set of control parameters;
- estimation of the system poles by means of the SSI algorithm;
- interpretation of the stabilization diagram (SD);
- confidence level assessment of the results.

Although the proper operation of the SSI algorithm largely depends on several control parameters, few efforts have been spent hitherto to avoid a manual selection. In fact, these control parameters are often fixed a priori as constant values or are obtained after a sensitivity analysis within given intervals, and their definition is ultimately based on subjective evaluations or personal experiences [e.g.6–8,14,20–24]. However, there are also some recent works that attempted to provide rationale guidelines for tuning automatically the control parameters of the SSI algorithm. For example, Priori et al. [25] proposed some rules to select the optimal values of the number of block rows and columns of the Hankel matrix collecting the output data as well as those for the number of block rows of the past output subpartition and the number of block rows of the future output subpartition in the SSI-data algorithm. Particularly, the minimum number of block rows of the Hankel matrix has been related to the number of cycles of the fundamental frequency. Next, the minimum number of block rows of the future output subpartition is associated with the modal characteristics of the structure and the sampling frequency. The proper setting of the lower bounds of the remaining control parameters is finally based on the amount of information that the algorithm takes into account for identifying the system (upper and lower bounds of the model order are instead assigned a priori, and the final value is defined as the minimum order at which the largest number of modes appear to be stable). Recently, Zini et al. [11] proposed a procedure to define the number of block rows in the Hankel matrix gathering all the output data and the range of variation of the model order in the SSI-cov algorithm. Herein, the minimum model order is first assumed as twice the number of modes estimated from a preliminary spectral analysis, and further increased by means of an amplifying coefficient. The maximum model order is calculated as the product between the minimum model order and an overmodelling coefficient. The maximum model order is then employed to estimate the upper and lower bounds of the number of block rows of the Hankel matrix. The final number of block rows in the Hankel matrix is obtained from a sensitivity analysis, and the maximum model order is also validated.

Once the control parameters are selected, the poles of the identified linear system are computed for each model order using the SSI algorithm (e.g., either SSI-cov or SSI-data). The estimated poles of the system are usually presented in a stabilization diagram (SD). Some poles will represent stable (i.e., physical) modes while others will correspond to spurious (i.e., numerical) modes. Indeed, spurious modes will inevitably appear owing to the fact that parametric models attempt to fit the noisy data as best as possible for an imposed conservative over-specification of the model order [3]. Since the amount of collected data from continuous monitoring can be very large, the manual interpretation of estimated poles is unfeasible and automatic procedures are required.

Most of the recent approaches for the automated interpretation of the SD are mainly based on a clustering technique that joints together stable poles with similar properties. This is by far the most investigated aspect within AOMA. Hierarchical clustering and partition clustering methods are the most common in the current literature. The hierarchical clustering technique considers all stable modes as separate clusters, and then groups two adjacent clusters in order to produce a new one. This procedure is repeated until the distances between the rest clusters are larger than a user-specified threshold. Partition clustering techniques tend to divide the stable modes into several clusters [26]. On the one hand, a critical issue in the application of hierarchical clustering methods is the selection of the threshold value of the distances between the rest clusters for which the iterative procedure is stopped. On the other hand, a critical issue in the application of partition clustering techniques is attributable to the fact that the number of clusters must be assigned in advance.

For instance, the clustering-based approach proposed by Reynders et al. [7] for the automated interpretation of the SD consists of the following steps: (i) a pre-cleaning stage by means of a classification of all the identified modes as possible physically or certainly spurious; (ii) hierarchical clustering of the possible physical modes for the automatic detection of vertical lines in the SD; (iii) final classification of the formed clusters. Some applications of the hierarchical clustering method for the automatic interpretation of the SD have been reported by Magalhaes et al. [6], de Almeida Cardoso et al. [16], Zonno et al. [27], and Garcia-Macias and Ubertini [28], among the others. Zini et al. [11] also proposed a statistical approach to define the cut-off threshold in the hierarchical clustering technique. As regards the partition clustering techniques, the k-means clustering (where the clusters are mutually exclusive) [7] and the fuzzy c-means clustering (where the clusters overlap) [5,9,19,29,30] have been adopted. For the sake of completeness, it is pointed out that hybrid clustering approaches have been also proposed [10,31]. For example, Mugnaini et al. [32] proposed the application of the k-means clustering to separate the poles that exhibit high stability from those that show low stability. Subsequently, hierarchical clustering was used to create clusters of poles with similar features. The k-means clustering was then applied once again to discern between highly and sparsely populated clusters, and the latter are discarded. Short reviews about clustering techniques for AOMA have been presented by Hasan et al. [33] as well as Chauhan and Tcherniak [34]. As a matter of fact, all these works that implement a clustering algorithm are instances of machine learning applications in AOMA. A different

way to integrate machine learning and AOMA has been presented recently by Liu et al. [35]. It is based on two neural networks [36]: while the first neural network is employed to determine the model order, the second one is used to identify the modal parameters.

Whichever way the identification is performed, the uncertainties at the origin propagate throughout the workflow and affect the final evaluation of the modal parameters as pointed out by Reynders et al. [37], who also provided a partial list of the sources of uncertainty. Some uncertainties are somehow irreducible, such as those due to nonlinearities and nonstationarity. The uncertainties due to the control parameters setting are reducible, but cannot be removed at all. Since the identification of the exact modal parameters is utopistic, it is thus important to assess the confidence in the final estimates (e.g., in terms of bounds, distributions, or statistical moments). Pintelon et al. [38] as well as Reynders et al. [37,39] are among the few who addressed this issue. To this end, they employ the first-order perturbation analysis to quantify how uncertainties propagate into the final results of the output-only modal analysis of structures. These studies, however, are not intended for automated applications. In this regard, because of the high influence of the control parameters on the final modal estimates, it would be especially important to also evaluate how the uncertainty inherent to their definition propagates in the AOMA.

This work would like to propose a new paradigm for the output-only identification of the modal features of structures and infrastructures subjected to ambient vibrations, the intelligent operational modal analysis (i-AOMA). The proposed approach implements the SSI-cov algorithm for modal identification and the overall procedure is basically divided into two steps. Quasi-random samples of the control parameters for the SSI-cov algorithm are generated during the first step. The SSI-cov algorithm is then performed for each sample and the corresponding SDs are elaborated in order to prepare a database for training the intelligent core of the i-AOMA method. This is a machine learning technique that predicts which combination of the control parameters for the SSI-cov algorithm is able to provide good modal estimates. In the second step, new quasi-random samples of the control parameters for the SSI-cov algorithm are generated repeatedly. If the generic sample is classified as feasible by the intelligent core of the i-AOMA method, then the SSI-cov algorithm is performed. Once a convergence criterion is achieved, final stable modal results of interest are distilled from the SDs, and relevant statistics are computed to evaluate their confidence level.

The current paper is organized as follows. Section 2 provides a brief overview of the SSI-cov algorithm and the role of its control parameters. The proposed i-AOMA method is then thoroughly presented in Section 3. This also includes the presentation of relevant implementation details of the corresponding code, which is made freely available. A preliminary numerical validation is presented in Section 4. The identification of the iconic Al Hamra Firduos Tower located in Kuwait City has been performed by means of the proposed i-AOMA method in Section 5. Finally, conclusive remarks about the advantages and limitations of the proposed approach are highlighted within Section 6.

2. Brief review about the stochastic subspace identification

2.1. Theoretical background

In agreement with most of the current literature, the SSI algorithm is considered for output-only automatic modal identification of linear structures under ambient vibrations. Although the proposed approach can be applied with any version, the SSI-cov algorithm is herein adopted. Actually, since the SSI-cov algorithm is faster and less memory intensive than the SSI-data algorithm [5,9,10,16], it is deemed especially appropriate in this context because it must be executed several times according to the proposed procedure. Henceforth, a short overview of the SSI-cov algorithm is provided in such a way to better introduce the control parameters that will be handled through the proposed machine-learning-based approach.

The state–space representation of the output-only vibration-based structural monitoring leads to the following discrete-time model:

$$\begin{aligned} \boldsymbol{x}_{r+1} &= \boldsymbol{A}\boldsymbol{x}_r + \boldsymbol{v}_r \\ \boldsymbol{y}_r &= \boldsymbol{C}\boldsymbol{x}_r + \boldsymbol{w}_r \end{aligned}, \tag{1}$$

where $\boldsymbol{x}_r \in \mathbb{R}^n$, $\boldsymbol{y}_r \in \mathbb{R}^l$, $\boldsymbol{A} \in \mathbb{R}^{n\times n}$ and $\boldsymbol{C} \in \mathbb{R}^{l\times n}$ are the state vector, the outputs vector, the state transition matrix and the observation matrix, respectively, for the rth sample. Moreover, l is the number of monitored degrees of freedom (DOFs) while n is the system order. The excitation $\boldsymbol{v}_r$ is the process noise and $\boldsymbol{w}_r$ is the measurement noise.

Let $\boldsymbol{Y} \in \mathbb{R}^{2il\times j}$ be the following block Hankel matrix of the output data:

$$\boldsymbol{Y} = \frac{1}{\sqrt{j}}\left[\begin{array}{cccc} \boldsymbol{y}_0 & \boldsymbol{y}_1 & \cdots & \boldsymbol{y}_{j-1} \\ \cdots & \cdots & \cdots & \cdots \\ \boldsymbol{y}_{i-2} & \boldsymbol{y}_{i-1} & \cdots & \boldsymbol{y}_{i+j-3} \\ \boldsymbol{y}_{i-1} & \boldsymbol{y}_i & \cdots & \boldsymbol{y}_{i+j-2} \\ \hline \boldsymbol{y}_i & \boldsymbol{y}_{i+1} & \cdots & \boldsymbol{y}_{i+j-1} \\ \boldsymbol{y}_{i+1} & \boldsymbol{y}_{i+2} & \cdots & \boldsymbol{y}_{i+j} \\ \cdots & \cdots & \cdots & \cdots \\ \boldsymbol{y}_{2i-1} & \boldsymbol{y}_{2i} & \cdots & \boldsymbol{y}_{2i+j-2} \end{array}\right]. \tag{2}$$

By means of Eq. (2), the block Toeplitz matrix $\boldsymbol{L}_i \in \mathbb{R}^{il\times il}$ is readily obtained as follows:

$$\boldsymbol{L}_i = \begin{bmatrix} \boldsymbol{\Lambda}_i & \boldsymbol{\Lambda}_{i-1} & \cdots & \boldsymbol{\Lambda}_1 \\ \boldsymbol{\Lambda}_{i+1} & \boldsymbol{\Lambda}_i & \cdots & \boldsymbol{\Lambda}_2 \\ \vdots & \vdots & \ddots & \vdots \\ \boldsymbol{\Lambda}_{2i-1} & \boldsymbol{\Lambda}_{2i-2} & \cdots & \boldsymbol{\Lambda}_i \end{bmatrix}, \tag{3}$$

where the entries are the output covariance matrices. The use of the Toeplitz matrix of output covariance matrices can reduce the computational effort during the modal identification, thereby improving the efficiency of the elaboration.

The matrix $\boldsymbol{L}_i$ can be decomposed into the corresponding observability and controllability matrices as follows:

$$\boldsymbol{L}_i = \begin{bmatrix} \boldsymbol{C} \\ \boldsymbol{C}\boldsymbol{A} \\ \vdots \\ \boldsymbol{C}\boldsymbol{A}^{i-1} \end{bmatrix} \begin{bmatrix} \boldsymbol{A}^{i-1}\boldsymbol{G} & \boldsymbol{A}^{i-2}\boldsymbol{G} & \dots & \boldsymbol{G} \end{bmatrix} = \boldsymbol{O}_i \boldsymbol{C}_i, \tag{4}$$

where $\boldsymbol{O}_i \in \mathbb{R}^{il \times n}$ is the so-called extended observability matrix and $\boldsymbol{C}_i \in \mathbb{R}^{n \times il}$ is the inversely extended controllability matrix.

It is known that $\boldsymbol{O}_i$ and $\boldsymbol{C}_i$ can be determined from $\boldsymbol{L}_i$ by reduced singular value decomposition:

$$\boldsymbol{L}_i = \boldsymbol{U}\boldsymbol{\Sigma}\boldsymbol{V}^{\top},\ \boldsymbol{O}_i = \boldsymbol{U}\boldsymbol{\Sigma}^{1/2},\ \ \boldsymbol{C}_i = \boldsymbol{\Sigma}^{1/2}\boldsymbol{V}^{\top}, \tag{5}$$

where $\boldsymbol{U} \in \mathbb{R}^{il \times 1}$, $\boldsymbol{\Sigma} \in \mathbb{R}^{il \times il}$ and $\boldsymbol{V} \in \mathbb{R}^{il \times 1}$ are the matrix of the left singular vectors, the singular values matrix and the matrix of the right singular vectors, respectively. Eq. (5) can be obtained by retaining only a given number of singular values and corresponding singular vectors. To this end, the SD is built by collecting all estimated modes by varying the retained number of singular values in Eq. (5).

Hence, the system matrices $\boldsymbol{A}$ and $\boldsymbol{C}$ can be identified as follows:

$$\boldsymbol{A} = (\boldsymbol{S}_2\boldsymbol{O}_i)^{\dagger}(\boldsymbol{S}_1\boldsymbol{O}_i), \tag{6a}$$

$$\boldsymbol{C} = \boldsymbol{S}_3\boldsymbol{O}_i. \tag{6b}$$

Herein, the symbol † denotes the Moore–Penrose pseudo-inverse whereas $\boldsymbol{S}_1$, $\boldsymbol{S}_2$ and $\boldsymbol{S}_3$ are the following selection matrices:

$$\boldsymbol{S}_1 = \begin{bmatrix} \boldsymbol{O}_{(i-1)l \times l} & \boldsymbol{I}_{(i-1)l} \end{bmatrix},\ \boldsymbol{S}_2 = \begin{bmatrix} \boldsymbol{I}_{(i-1)l} & \boldsymbol{0}_{(i-1)l \times l} \end{bmatrix},\ \boldsymbol{S}_3 = \begin{bmatrix} \boldsymbol{I}_l & \boldsymbol{0}_{l \times (i-1)l} \end{bmatrix}. \tag{7}$$

The system's modal parameters (i.e., eigenfrequencies, damping ratios, and mode shapes) can be thus estimated from the identified system matrices $\boldsymbol{A}$ and $\boldsymbol{C}$. First, the eigenvalue decomposition of $\boldsymbol{A}$ leads to the diagonal matrix $\boldsymbol{\Lambda}$ of discrete-time system poles λ_u and corresponding right eigenvectors $\boldsymbol{\psi}_u$:

$$\boldsymbol{A} = \boldsymbol{\Psi}\boldsymbol{\Lambda}\boldsymbol{\Psi}^{-1},\ \boldsymbol{A}\boldsymbol{\psi}_u = \lambda_u \boldsymbol{\psi}_u, \tag{8}$$

where $1 \le u \le m$, being m the total number of eigenvalues of interest. The undamped eigenfrequencies f_u and the damping ratios ξ_u (in %) are finally determined as follows:

$$\lambda_{cu} = \frac{\ln(\lambda_u)}{\Delta t},\ f_u = \frac{|\lambda_{cu}|}{2\pi},\ \xi_u = -100\frac{\Re\mathfrak{e}(\lambda_{cu})}{|\lambda_{cu}|}, \tag{9}$$

where λ_{cu} are the continuous-time system poles, Δt is the sampling interval, $|\cdot|$ denotes the complex modulus and $\Re\mathfrak{e}(\lambda_{cu})$ is the real part of λ_{cu}. The real part of the eigenvectors $\boldsymbol{\psi}_u$ instead leads to the experimental mode shapes $\boldsymbol{\phi}_u$:

$$\boldsymbol{\phi}_u = \Re\mathfrak{e}(\mathbf{C}\boldsymbol{\psi}_u). \tag{10}$$

2.2. Control parameters

The previous short survey about the SSI-cov algorithm highlights that it is governed by the following control parameters:

- the number of block rows i (also known as time shift);
- the length of the data time windows j;
- the model order n.

Ultimately, the efficiency and accuracy of the SSI-cov algorithm depend on the proper selection of i, j, and n.

It is noted that these control parameters are not independent of each other. Particularly, a system of order n can be identified as far as the following condition is fulfilled [3]:

$$il \ge n. \tag{11}$$

Furthermore, it has been shown [40] that the variance of the estimates initially decreases when i increases because a larger amount of noise is rejected. Conversely, splitting phenomena occur for too high values of i, and the resulting mathematical modes lead to a bias in the physical pole estimates. Such evidence implies that the value of i cannot be set as large as possible. Finally, it is theoretically required that $j \to \infty$. In reality, this requirement can be only approximated since the output signals are always finite in length.

Indeed, the reliable and efficient execution of the SSI-cov algorithm requires that i and j are fixed consistently with n by taking also into account computational effort and memory usage.

3. Intelligent automatic operational modal analysis

3.1. General outline

A machine-learning-based strategy has been conceived in the present work to deal with the output-only automatic modal identification of linear structures under ambient vibrations via SSI-cov.

The proposed approach for the intelligent automatic operational modal analysis (i-AOMA) moves from a recent study by Zhou et al. [41,42], who introduced a Monte Carlo (MC) simulations-based construction of the SD for SSI algorithms. Specifically, MC simulations are performed by sampling randomly the length of the data time window $j \in [j_{min}, j_{max}]$ and the maximum model order $n \in [n_{min}, n_{max}]$. The time window j is centered symmetrically with respect to a randomly generated time instant $t \in [0, j_{max}]$. The underlying assumption by Zhou et al. [41,42] is that, in a statistical sense, spurious modes occur occasionally while physical modes occur recurrently. Accordingly, a stability check is performed in order to discriminate the poles denoting the physical modes from those representing spurious modes over s simulations (it is noted that each simulation corresponds to one application of the SSI-cov algorithm). The resulting SD is finally processed via the k-means clustering technique to determine the structural modal parameters.

The methodology proposed by Zhou et al. [41,42] is attractive, but the following issues can also be recognized.

- The time shift i is still considered a user-defined parameter. Given the relevance of such control parameter, the manual tuning of its value is an impediment towards accurate automatic applications.
- The number of MC simulations s is a new user-defined parameter that plays a somehow important role. However, neither motivations nor guidelines are given about its selection.
- The intervals of the control parameters for Monte Carlo simulations must be defined carefully. Otherwise, several random samplings might result into an ill-conditioned application of the SSI algorithm, also leading to numerical failures or excessive elaboration time. This, in turn, also reflects on the final results, which can actually be carried out from a too low number of samples.
- The MC simulations-based construction of the SD is analyzed in order to derive a deterministic estimation of the modal parameters. So doing, any information about the confidence level of the final estimates due to the different combinations of the control parameters is lost.

The proposed novel approach relies on the MC simulations-based construction of the SD for SSI algorithms presented by Zhou et al. [41,42], which is largely revised by means of a machine-learning-driven strategy designed to overcome all these limitations. In its essence, it is organized as follows.

- *Database preparation and training of the intelligent core (i-AOMA Phase 1).* Quasi-random samples of the control parameters for the SSI-cov algorithm are generated. The SSI-cov algorithm is then performed for each sample and the corresponding SDs are elaborated in order to prepare a database for training the intelligent core of the i-AOMA method. This is a machine learning technique that predicts which combination of the control parameters for the SSI-cov algorithm is able to provide good modal estimates.
- *Machine-learning-driven automatic identification and uncertainty propagation (i-AOMA Phase 2).* New quasi-random samples of the control parameters for the SSI-cov algorithm are generated repeatedly. If the generic sample is classified as feasible by the intelligent core of the i-AOMA method, then the SSI-cov algorithm is performed. Once a convergence criterion is achieved, final stable modal results of interest are distilled from the SDs, and relevant statistics are computed to evaluate their confidence level.

3.2. Analysis of the stabilization diagram via Kernel Density Estimation (i-AOMA Phase 1a)

The Halton technique [43,44] is adopted to generate quasi-random samples of the control parameters for the SSI-cov algorithm within the corresponding ranges. They are the maximum model order n, the time window length j, the time target t with respect to which the time window is centered [42], and the time shift parameter i. Taking into consideration the existing literature [40,42,45], the bounded ranges for $\{n, j, t, i\}$ are defined as follows:

$$n \in \left[n_{min}, n_{max}\right] = \left[2 \cdot l, i_{max} \cdot l\right], \tag{12}$$

$$j \in \left[j_{min}, j_{max}\right] = \left[\left\lfloor \frac{2}{\max\{f_f, 1\}} \right\rceil, j_{max} \cdot l\right], \tag{13}$$

$$t \in \left[t_{min}; t_{max}\right] = \left[0, j_{max}\right], \tag{14}$$

$$i \in \left[i_{min}, i_{max}\right] = \left[\left\lfloor \frac{f_s}{2\max\{f_f, 1\}} \right\rceil, 10 \left\lfloor \frac{f_s}{2\max\{f_f, 1\}} \right\rceil\right], \tag{15}$$

where $\lfloor \cdot \rceil$ is the rounding operation to the nearest integer and f_f the fundamental frequency (which is estimated by means of the singular value decomposition of the power spectral density as suggested by Zhou and Li [42]).

A database is then prepared for training the intelligent core of i-AOMA. To this end, s successful quasi-MC simulations are performed: each simulation corresponds to an application of the SSI-cov algorithm using a sample of control parameters generated

according to the bounds listed in Eqs. (12)–(15) by means of the Halton technique. This database is prepared by assuming $s \geq 100$ as suggested by Zhou and Li [42].

It is pointed out that the user's intervention is limited to roughly defining the ranges of the control parameters $\{n, j, t, i\}$, even if their reasonable definition as per Eqs. (12)–(15) is useful to enhance the efficiency of the i-AOMA. After the training stage, in fact, the intelligent core of i-AOMA will detect the combinations of the control parameters $\{n, j, t, i\}$ that are likely to produce satisfactory results by means of the SSI-cov algorithm. Similarly, the combinations of the control parameters that cause the premature stop of the SSI-cov algorithm because of numerical failure or excessive elaboration time (herein assumed equal to 30 s) are not discarded since they will serve to train the intelligent core of i-AOMA in recognizing unuseful combinations of the control parameters $\{n, j, t, i\}$. Furthermore, only a reasonable value for s is required in such a way to properly train the intelligent core of i-AOMA, but an automatic procedure will be introduced to determine how many quasi-MC simulations must be carried out in order to get the final modal estimates and to calculate the corresponding confidence level.

The SDs resulting from the s successful quasi-Monte Carlo simulations are then overlapped. So doing, a single comprehensive SD is obtained and, for each pole, a stability check is performed in terms of frequency, damping ratio, and mode shapes, in such a way to identify those corresponding to possibly physical modes. The following stability criteria are considered [3]:

$$\Delta f = \frac{f_a - f_b}{f_a} \leq 0.01 \tag{16}$$

$$\Delta \xi = \frac{\xi_a - \xi_b}{\xi_a} \leq 0.05 \tag{17}$$

$$1 - \mathrm{MAC}(\psi_a, \psi_b) \leq 0.02 \tag{18}$$

$$\xi_a \leq 0.1 \tag{19}$$

where the subscripts a, b represent two whichever poles in the SD, and MAC is the modal assurance criterion (which represents the measure of the correlation between two modal vectors [3]). Particularly, Eqs. (16)–(18) are denoted as soft criteria (SC) in terms of frequency, damping, and mode shape, respectively, whereas Eq. (19) is designated as hard criterion (HC) on the damping range [11].

The extraction of certainly physical poles (i.e., the identification of the most recurrent modes having physical meaning) from possibly stable poles (i.e., the poles that fulfill all stability criteria in Eqs. (16)–(19)) is not performed as most common by means of a traditional clustering procedure. Instead, this is accomplished via Kernel Density Estimation (KDE). The KDE aims at providing a nonparametric estimation of probability density functions (PDFs) directly from data [46]. Specifically, the KDE is an evolution of any naive estimator because it is based on a symmetric kernel function $K(-z) = K(z)$ that satisfies the following conditions [47,48]:

$$\int_{-\infty}^{+\infty} K(z)\mathrm{d}z = 1, \tag{20}$$

$$K(z) \geq 0. \tag{21}$$

The most common kernel is the Gaussian one [47,48]. In this context, the data consists of all the possible stable poles N_p within the comprehensive SD, which are considered as a univariate dataset along the frequency axis only. Therefore, the univariate KDE based on a Gaussian kernel can be written as follows:

$$\hat{\varphi} = \frac{1}{N_p h} \sum_{p=1}^{N_p} K\left(\frac{z - z_p}{h}\right), \tag{22}$$

where

$$K\left(\frac{z - z_p}{h}\right) = \frac{1}{\sqrt{2\pi h}} \mathrm{e}^{-\frac{(z-z_p)^2}{2h}}. \tag{23}$$

The parameter h in Eqs. (22)–(23) is known as bandwidth (BW) or smoothing parameter, and it is normally fixed across the entire sample [47].

The optimal choice of the BW is challenging because it rules the spread of the kernel, and thus the complexity of the resultant density estimate. Its optimal value represents a variance-bias trade-off between over-smoothed densities at high values of BW (which are not able to capture multi-modality properties) and excessively noisy densities at low values of BW (which present useless spurious fine structures [47,49]).

Since the BW definition has a significant impact, a user-dependent definition of its value should be avoided in automatic applications. Therefore, the improved Sheather–Jones (ISJ) algorithm [49,50] is performed to facilitate the automatic definition of the BW. This method is especially suitable when data are expected to be multimodal and far from Gaussian normality. Moreover, in order to analyze the performance of any KDE, error criteria are usually set to verify both punctual and global convergence to the real density $\varphi(\cdot)$ of the density estimation $\hat{\varphi}(\cdot; h)$. An appropriate global indicator of their $\mathcal{L}_2$ distance is represented by the mean integrated squared error (MISE), which is defined as follows [49]:

$$\mathrm{MISE}\left[\hat{\varphi}(\cdot, h)\right] = \mathbb{E} \int \left(\hat{\varphi}(z; h) - \varphi(z)\right)^2 \mathrm{d}z, \tag{24}$$

where $\mathbb{E}$ denotes the expected value.

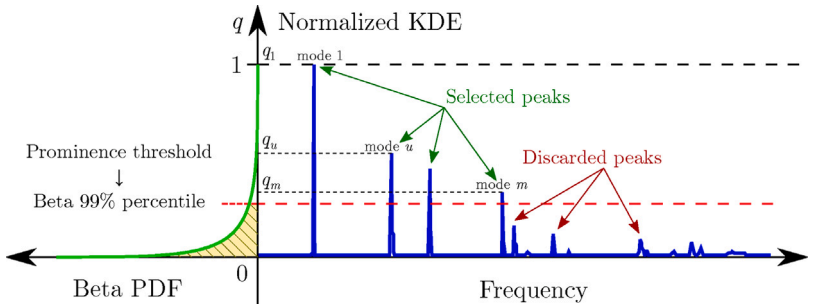

Fig. 1. Statistical-based criterion for the automatic definition of the prominence threshold and the detection of significant peaks from the normalized KDE.

The ISJ algorithm is mainly based on the minimization of the asymptotic MISE, which recursively produces sequences of BW estimates [50]. It is highlighted that the direct implementations of the KDE algorithms might be computationally expensive in the magnitude of $\mathcal{O}(N_p^2)$ or even larger [46]. This evidence motivated the development of some approximated implementations in the past years. Specifically, the adopted KDE algorithm relies on the discrete convolution workflow provided by the Fast Fourier Transform (FFT-KDE). This is implemented by exploiting the symmetry of the chosen Gaussian kernel function to reduce the computational effort [51]. Particularly, a uniform discrete grid of M points is used to bin the N_p stable poles, thus achieving an overall complexity of $\mathcal{O}(N_p 2^1 + M \log M)$ [49]. For better controlling the granularity of the grid, in the current study, M is set equal to $\lfloor 1000 \cdot f_s/2 \rceil$, being f_s the sampling frequency of the signals.

The KDE plays a crucial role in post-processing the overlapped SDs. In fact, it allows detecting recurrent and significant patterns of stable poles' alignments only (i.e., certainly physical modes) from possibly stable poles, thus acting as a filter for the actual modal parameters. Indeed, the actual natural frequencies are located at the m peaks of interest in the normalized KDE (which is obtained by scaling the KDE in such a way that its largest value is equal to one). In order to automatize the extraction of certainly physical modes, only those stable poles around the m peaks of the normalized KDE within a distance equal to b_w times the BW h are retained, being b_w a factor governing the severity of the filtering effect of the poles of interest. The retaining bands are thus defined as follows:

$$\left[f_u - b_w \cdot h, f_u + b_w \cdot h\right]_u \quad (\text{with } u = 1, \dots, m), \tag{25}$$

where m is the total number of peaks of interest and f_u is the natural frequency associated with the uth peak. The value of b_w is the minimum integer number for which all the m groups of certainly stable poles are not empty.

A prominence-based criterion is employed to detect the m peaks of interest within the normalized KDE. Specifically, only the peaks above a prominence threshold are considered because they are attributable to physical modes. Conversely, the peaks below the prominence threshold are discarded. A statistical approach is proposed to setup automatically the prominence threshold value. By observing that the values of the normalized KDE lie within the bounded range $[0, 1]$, all the peak values are fitted through the Beta distribution with parameters α and β, denoted as $\mathcal{B}(\alpha, \beta)$. The maximum likelihood estimation algorithm is here employed for this task. It is noted that the normalized KDE will exhibit a few spiky peaks due to highly recurrent physical modes while it is equal to or close to zero otherwise: therefore, the fitted $\mathcal{B}(\alpha, \beta)$ is expected to be very squashed towards the zero of the normalized KDE (i.e. $\alpha \ll \beta$). The adopted statistical-based criterion for the selection of the prominence threshold is illustrated in Fig. 1.

It is worth highlighting that such prominence-based criterion implies a statistically-based discrimination between physical modes and spurious modes. In fact, let q be the generic peak value of the normalized KDE and q_u the corresponding value associated to a certainly physical mode u (where $1, \dots, m$ is the set of all the labels associated to the physical modes of interest of the structure). Then, the proposed prominence-based criterion is equivalent to the application of the following condition:

$$u(q_u) \in \{1, \dots, m\} \iff \int_0^{q_u} f_{\mathcal{B}}(q;\, \alpha, \beta)\, \mathrm{d}q \geq 1 - p_f, \tag{26}$$

where $f_{\mathcal{B}}$ denotes the Beta distribution probability density function. The prominence threshold is ruled by p_f, which defines the threshold probability of failure (i.e., the acceptable probability of extracting a spurious mode rather than a physical mode). In the present work, it is assumed $p_f = 1\%$, which means that the prominence threshold is the value corresponding to the 99th percentile in the fitted Beta distribution. This, in turn, implies that the chance of considering a spurious mode within the final set of the physical modes of interest $\{1, \dots, m\}$ is required to be no larger than 1%. It is evident that the larger p_f, the larger is m, but the larger is also the probability of considering spurious modes within the final set of m modes. The vice versa holds for low values of p_f.

3.3. Training of the intelligent core based on random forest technique (i-AOMA Phase 1b)

The number of successful quasi-MC simulations s has been defined arbitrarily. Although this value can be assumed very large to achieve a predefined convergence criterion, this strategy would be a waste of computational effort because some combinations of the control parameters are likely to produce poor results. Hence, the outcomes of all the previous simulations (i.e., successful and

aborted simulations) are considered to fill a training database for a random forest (RF) algorithm, which acts as an intelligent core of the proposed i-AOMA method. Specifically, the RF algorithm will be required to predict whether a new combination of the control parameters is able to provide enough useful modal information by producing as many certainly stable poles as possible within the retaining bands defined in Eq. (25).

A suitable metric must be associated with each previous k-tuple of the control parameters within the database in order to quantify objectively its goodness. To this end, an information content index IC is thus computed for each previous k-tuple of the control parameters $\{n, j, t, i\}_k$. It is defined as the ratio between the number of certainly stable poles $N^*_{p,k}$ (i.e., the number of stable poles falling within the retaining bands in Eq. (25)) and the total number of stable poles of the kth SD $N_{p,k}$, that is:

$$\mathrm{IC}_k = \frac{N^*_{p,k}}{N_{p,k}}. \tag{27}$$

So doing, it is possible to associate a quality index IC_k to each previous k-tuple of the control parameters $\{n, j, t, i\}_k$. In fact, IC_k is equal to one if the kth set of control parameters provides a SD where all the stable poles are retained because they fall within the KDE-based retaining bands in Eq. (25). Conversely, it is equal to zero if the set of kth control parameters provides a SD where no stable pole falls within the KDE-based retaining bands in Eq. (25) (IC_k is also equal to zero by default for the combinations of the control parameters that lead to a numerical failure or an excessive elaboration time). The main advantage of the metric in Eq. (27) is attributable to its simplicity since the implementation does not require further control parameters and is based on a simple counting procedure. This avoids growing the computational burden. However, other metrics (or a combination thereof) can possibly be adopted.

It is evident that the optimum computational effort is achieved when the analysis is performed for those combinations of the control parameters $\{n, j, t, i\}_k$ that corresponds to a high value of IC_k while those for which $\mathrm{IC}_k \approx 0$ are almost useless. It is assumed that if IC_k is less than a threshold value $\mathrm{IC}_{th} = 0.10$, then the corresponding set of control parameters $\{n, j, t, i\}_k$ is unfeasible because it is non-informative of the actual modal properties of the structure. Conversely, if IC_k is equal to or larger than a threshold value $\mathrm{IC}_{th} = 0.10$, then the corresponding set of control parameters $\{n, j, t, i\}_k$ is feasible because it provides enough information about the actual modal properties of the structure.

The RF algorithm is thus trained to classify each freshly generated set of the control parameters $\{n, j, t, i\}_k$ as either feasible or unfeasible, without performing the SSI-cov algorithm. Boolean discrimination is adopted such that the k-tuple of the control parameters $\{n, j, t, i\}_k$ is labeled with 1 if $\mathrm{IC}_k > \mathrm{IC}_{th}$ (feasible set of control parameters) and 0 otherwise (unfeasible set of control parameters). Boolean labeling improves the diversity among the most and the less informative sets of control parameters.

The RF algorithm is one of the most powerful and robust, yet simple, machine learning algorithms for classification problems [52]. Briefly, RF is an ensemble machine learning technique based on the simultaneous training of a group of various decision trees (weak learners), whose predictions are finally aggregated with a majority voting method [53]. The RF algorithm adopts an initial bagging procedure (also known as bootstrap), which is performed by randomly drawing a number of samples with replacements from the training set. A subset of input features is then used to train each decision tree component [52]. The usual size of this subset is $\sqrt{d}$, where d is the dimension of the features vector. Each decision tree component is trained in order to maximize the information gain [53], in such a way to look for the best features among the selected subset, thereby improving the tree diversity. The greatest advantage of any ensemble method is based on the adoption of a final majority voting system, which ensures a consistent level of accuracy and robustness in contrast to any single weak learner alone. The aggregation provides, in general, better results and reduces both bias and variance. This, in turn, improves the generalization capabilities and drastically mitigates any possible overfitting issue [52].

The use of the RF is especially attractive to enhance the automation level of the i-AOMA because it does not require careful tuning of its hyperparameters value by virtue of the intrinsic robustness due to its ensemble nature [53]. The only significant control parameter of the RF algorithm is the number of decision trees composing the forest: if it is high, then it would provide better results, with the side-effect of increasing the computation cost.

In the present study, the RF algorithm is implemented by considering 100 trees, an information gain measure based on the Gini impurity index, no depth tree pruning, and a maximum number of features for the bootstrap subset equal to $\sqrt{d} = 2$ (being $d = 4$ the size of the each k-tuple of the control parameters $\{n, j, t, i\}_k$).

3.4. Machine-learning-driven automatic identification and uncertainty propagation (i-AOMA Phase 2)

The Halton technique is employed to sample new k-tuples of the control parameters $\{n, j, t, i\}_k$ within the bounds listed in Eqs. (12)–(15). Then, the trained RF applies as an intelligent core in order to classify the newly generated k-tuple of the control parameters $\{n, j, t, i\}_k$: if it is classified as unfeasible, then the SSI-cov does not apply and a new set is considered. This allows to save elaboration time since only feasible k-tuples of the control parameters $\{n, j, t, i\}_k$ are processed henceforth. This intelligence-driven procedure is reaped until a suitable convergence criterion is achieved.

The convergence check is performed periodically considering a batch size of successful quasi-MC simulations b (i.e., convergence check of i-AOMA is performed every successful b runs of the SSI-cov algorithm). The selected convergence criterion depends on the uncertainty associated with the estimated mode shapes $\boldsymbol{\phi}_u = \begin{bmatrix}\phi_{u,1} & \dots & \phi_{u,l}\end{bmatrix}^{\mathrm{T}}$, which are carried out for $u = 1, \dots, m$ from the selected poles within the retaining bands defined in Eq. (25) on the basis of the normalized KDE. The mode shape vectors $\boldsymbol{\phi}_u$ are

Algorithm 1 Pseudocode of i-AOMA Phase 1 – Database preparation and training of the intelligent core

```
Define s                                                          ▷ Successful runs of the SSI-cov for training the RF algorithm
Define n_max, j_min, j_max, i_min, i_max                          ▷ Reasonable control parameters bounds
Generate quasi-random samples of the control parameters {n, j, t, i}_{k=1,...}
while s successful runs of SSI-COV are not completed do
    try
        @check execution time ≤ 30 s                              ▷ Admissible elaboration time
        SSI-cov({n, j, t, i}_k)                                   ▷ Compute the SD via SSI-cov
        Normalize mode shapes
    except                                                        ▷ Numerical failure, execution time larger than 30 s
        Set IC_k = 0                                              ▷ Unfeasible set of control parameters
end while
Overlap all the SDs
Check the poles stability                                         ▷ Detect possibly stable poles
Perform KDE                                                       ▷ Perform FFT-KDE with ISJ algorithm
Recognize certanly stable poles from the normalized KDE
Calculate IC_k
Set IC threshold IC_th, if IC_k ≥ IC_th then IC_k = 1 else IC_k = 0
Classifier training RF.fit(inputs= {n, j, t, i}_{k=1,...},targets= {IC_k}_{k=1,...})
```

thus considered as multivariate random vectors, and the overall uncertainty is assessed by means of the generalized sample variance matrix $\boldsymbol{S}_u$ (i.e, a covariance matrix of the components of the uth mode shape vector $\boldsymbol{\phi}_u$), which is defined as follows [54]:

$$\boldsymbol{S}_u = \begin{bmatrix} \mathbb{V}\mathrm{ar}\left[\phi_{u,1}\right] & \mathbb{C}\mathrm{ov}\left[\phi_{u,1},\phi_{u,2}\right] & \dots & \mathbb{C}\mathrm{ov}\left[\phi_{u,1},\phi_{u,l}\right] \\ & \mathbb{V}\mathrm{ar}\left[\phi_{u,2}\right] & \dots & \vdots \\ & & \ddots & \mathbb{C}\mathrm{ov}\left[\phi_{u,l-1},\phi_{u,l}\right] \\ \text{Sym.} & & & \mathbb{V}\mathrm{ar}\left[\phi_{u,l}\right] \end{bmatrix}. \tag{28}$$

This is a symmetric matrix collecting the sample variances ($\mathbb{V}\mathrm{ar}[\cdot]$) of the $\boldsymbol{\phi}_u$'s components on the main diagonal, whereas the sample covariances ($\mathbb{C}\mathrm{ov}[\cdot,\cdot]$) outside of the main diagonal are computed among pairs of $\boldsymbol{\phi}_u$'s components. A suitable measure of the overall variability of a multivariate random vector is the total sample variance, which corresponds to the trace of the matrix $\boldsymbol{S}_u$ [54], namely $\mathrm{tr}(\boldsymbol{S}_u)$. Hence, the traces of the sample covariance matrices given by Eq. (28) for $u = 1, \dots, m$ are computed, and the acceptable shifting convergence band rule (ASCBR) [55,56] is employed to limit the subjective judgment of the convergence condition. The batch size is taken $b = 50$ [56] whereas the intelligence-driven procedure is stopped (i.e., new samples of the control parameters are no longer generated) once the relative total sample variance for each mode of interest $\{\Delta\mathrm{tr}(\boldsymbol{S}_u)\}_{u=1}^{m}$ is restricted to $\pm 2\%$ [57].

Once the convergence is achieved, the SDs carried out from all the applications of the SSI-cov algorithm are overlapped, and the stability criteria in Eqs. (16)–(19) apply to identify possibly physical modes. Thereafter, the normalized KDE-based filtering procedure is performed once again to retrieve the final estimates of the modal parameters, and basic statistics are determined. These statistics allow quantifying the epistemic uncertainty in the final modal estimates due to the variability of the control parameters.

As far as the uncertainty quantification for the estimated mode shapes, a boxplot-based representation is recommended [58,59]. So doing, the boxplot's whiskers represent the distance between the first quartile or the third quartile of the modal displacement with respect to the lower and upper fence, respectively. The fences, in turn, are located at an additional distance of 1.5 times the interquartile range. The whiskers-based representation is deemed appropriate since it provides a robust and not necessarily symmetric measure of the uncertainty level.

3.5. Implementation details and open-source code

The workflows for both Phase 1 and Phase 2 of the i-AOMA method are depicted in Fig. 2. Algorithms 1 and 2 provides the pseudocode for Phase 1 and Phase 2 of the i-AOMA method, respectively.

The proposed i-AOMA method has been implemented by means of the Python programming language. Particularly, the implementation of i-AOMA relies on PyOMA [4], which is a suite of Python libraries for standard output-only modal identification of linear structures. The code implementation is based on the extensive use of the object-oriented programming paradigm in order to make the elaboration as fast as possible. The elaboration time can be dramatically reduced by means of a suitable parallelization of the elaboration tasks.

The code is available at the following Google Colab notebook link: https://colab.research.google.com/drive/1D6z1zM7lqJavI6yyMCI8BMnEqV9zw7kW?usp=sharing. It can also downloaded from the following GitHub repository: https://github.com/marco-rosso-m/i-AOMA.

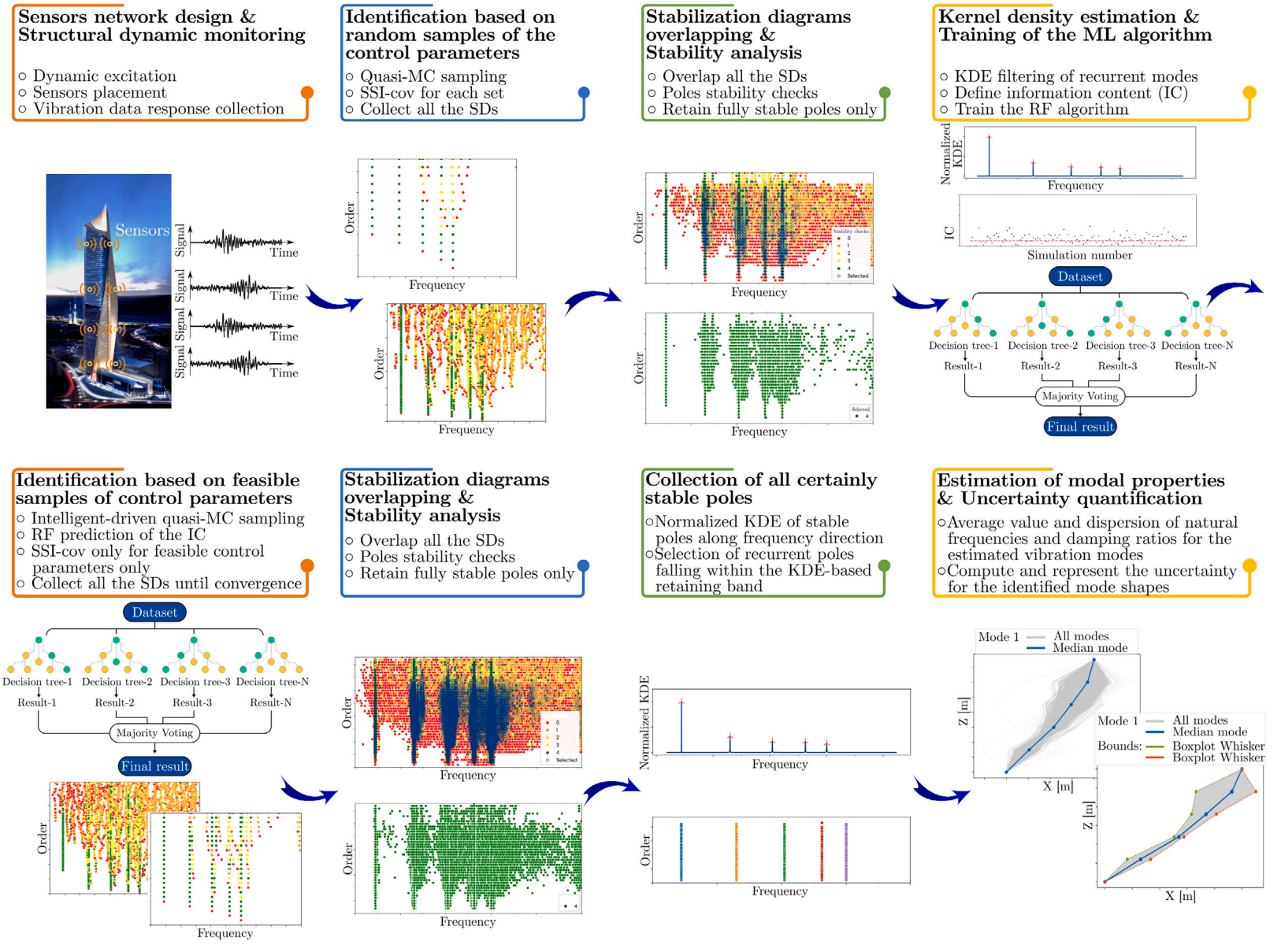

Fig. 2. The i-AOMA workflow: i-AOMA Phase 1 (top row) and i-AOMA Phase 2 (bottom row).

Algorithm 2 Pseudocode of i-AOMA Phase 2 – Machine-learning-driven automatic identification and uncertainty propagation

```
Set the batch size b = 50                                          ▷ Convergence check every 50 runs of the SSI-cov
Set a large number s_max
Generate quasi-random samples of the control parameters {n, j, t, i}_{k=1}^{s_max}
while k ≤ s_max and {Δtr(S_u)}_{u=1}^{m} ≥ ±2% do
    try
        if RF.predict(inputs= {n, j, t, i}_k) = 1 then             ▷ RF classification
            @check execution time ≤ 30 s                           ▷ Admissible elaboration time
            SSI-cov({n, j, t, i}_k)                                ▷ Compute the SD via SSI-cov
            Normalize mode shapes
            if k reaches multiples of b then
                Overlap all the SDs up to k runs
                Check the poles stability                          ▷ Detect possibly stable poles
                Perform KDE                                        ▷ Perform FFT-KDE with ISJ algorithm
            end if
        else
            Set IC_k = 0                                           ▷ Unfeasible set of control parameters
        end if
    except                                                         ▷ Numerical failure, execution time larger than 30 s
        Set IC_k = 0                                               ▷ Unfeasible set of control parameters
end while
Overlap all the SDs
Check the poles stability                                          ▷ Detect possibly stable poles
Perform KDE                                                        ▷ Perform FFT-KDE with ISJ algorithm
Select certainly stable poles from the normalized KDE
Compute basic statistics of the physical modal parameters of interest
```

4. Validation: numerical benchmark case

The proposed i-AOMA method is initially tested on a numerical benchmark problem following Pasca et al. [4]. A 5 degrees-of-freedom (DOF) shear-type planar frame under white noise excitation is considered, with lumped mass at each floor equal to 25.91 Ns^2/mm and story stiffness equal to 10,000 N/mm for every floor level. The damping matrix is computed by assuming a constant damping ratio equal to 2% for every mode. System frequencies and mode shapes (normalized with respect to the largest value) are the following:

$$\boldsymbol{f} = \begin{bmatrix} f_1 \\ f_2 \\ f_3 \\ f_4 \\ f_5 \end{bmatrix} = \begin{bmatrix} 0.88995 \\ 2.59776 \\ 4.09511 \\ 5.2607 \\ 6.0001 \end{bmatrix} \text{ Hz}, \tag{29}$$

$$\boldsymbol{\Phi} = [\boldsymbol{\phi}_1\ \boldsymbol{\phi}_2\ \boldsymbol{\phi}_3\ \boldsymbol{\phi}_4\ \boldsymbol{\phi}_5] = \begin{bmatrix} 0.28463 & -0.763521 & 1 & 0.918986 & -0.5462 \\ 0.5462 & -1 & 0.28463 & -0.763521 & 0.918986 \\ 0.763521 & -0.5462 & -0.918986 & -0.28463 & -1 \\ 0.918986 & 0.28463 & -0.5462 & 1 & 0.763521 \\ 1 & 0.918986 & 0.763521 & -0.5462 & -0.28463 \end{bmatrix}. \tag{30}$$

Vibration response data at every DOF corresponding to 1 h recordings have been generated with a sampling frequency of $f_s = 100$ Hz. The response data have been polluted by adding a white noise with a signal-to-noise ratio equal to 10% in order to reproduce real-world monitoring conditions. Following Pasca et al. [4], synthetic monitoring data have been decimated with a factor equal to 5 after the application of a finite impulse response anti-aliasing low-pass filter with a 30 points Hamming window. Fig. 3 illustrates synthetic monitoring data and the singular value decomposition of the power spectral density.

The singular value decomposition of the power spectral density shows that the fundamental frequency is $f_f = 0.890$ Hz. Hence, the bounds of the control parameters are roughly defined according to Eqs. (12)–(15). A total of $s = 100$ quasi-random samples of the control parameters have been generated according to the Halton technique for the present benchmark case during the i-AOMA phase 1. To this end, 220 sets of control parameters have been sampled to gather $s = 100$ successful applications of the SSI-cov algorithm, thus resulting in a success rate of about 45%. Numerical failure or excessive elaboration time occurred for the remaining 120 samples. Once the SDs corresponding to $s = 100$ successful applications of the SSI-cov algorithm have been overlapped, stability checks have been performed according to Eqs. (16)–(19) and possibly stable poles are then identified. The FFT-KDE algorithm has

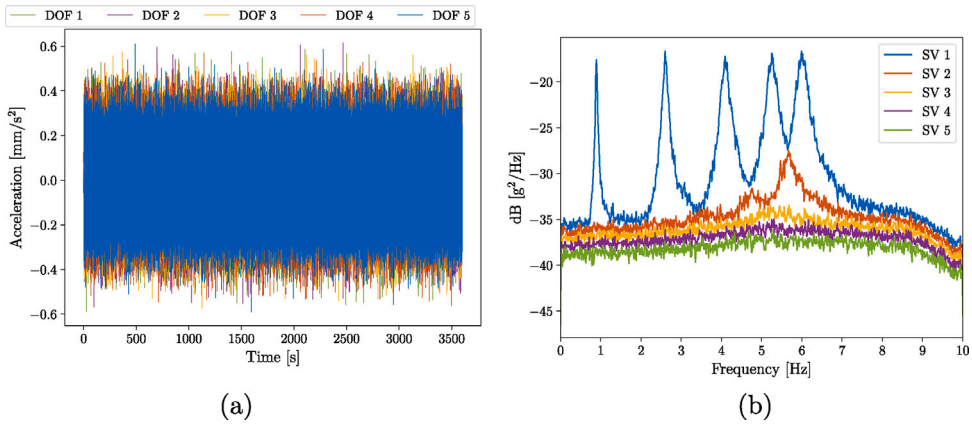

Fig. 3. Numerical benchmark case: synthetic monitoring data (a) and singular value decomposition of the power spectral density (b).

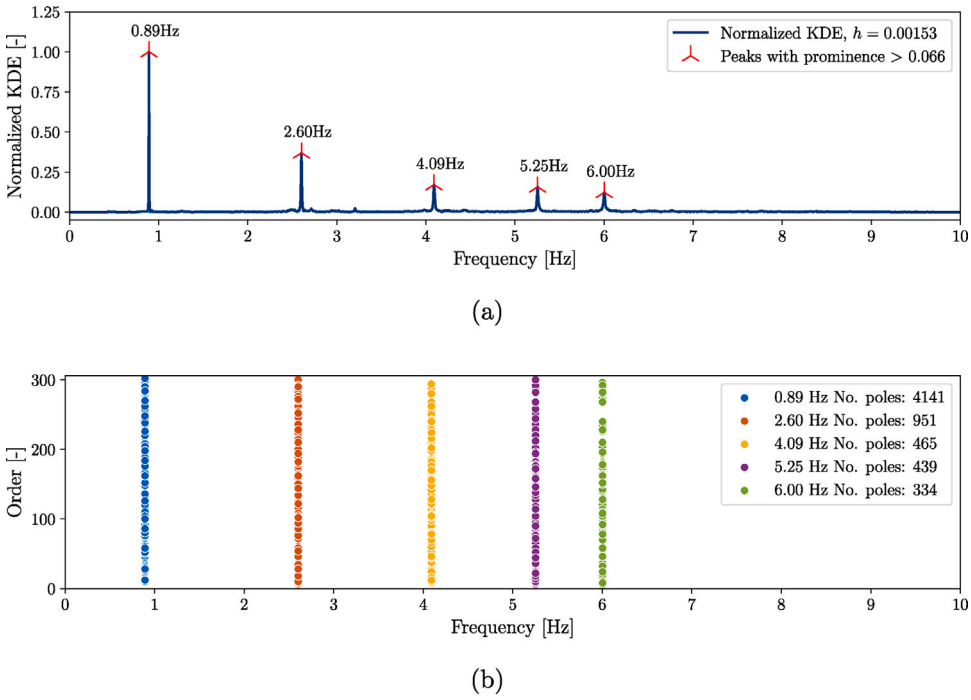

Fig. 4. Numerical benchmark case i-AOMA phase 1: normalized KDE together with the identified peaks (a) and certainly stable poles falling within the retaining bands (b) obtained from the sets of control parameters generated for training the intelligent core of i-AOMA.

been next applied on these possibly stable poles, delivering an estimate of the BW equal to 0.0015 Hz with the ISJ algorithm. The statistical value of the prominence threshold for the peaks' identification from the normalized KDE (99th percentile in the fitted Beta distribution) is equal to 0.066. A factor of $b_w = 1$ has been automatically identified to successfully collect non-empty groups of stable poles around the peaks of the normalized KDE according to Eq. (25). Subsequently, the database consisting of all the generated control parameters and the corresponding IC values is prepared in order to train the intelligent core of the i-AOMA method, i.e. the RF algorithm. Figs. 4–5 illustrate the main results obtained from the $s = 100$ sets of control parameters generated during the i-AOMA phase 1.

Henceforth, new quasi-random samples of the control parameters are generated with the Halton technique. However, the SSI-cov analysis is now performed only for those samples that are classified as feasible by the RF algorithm. In total, the algorithm generated new 2105 samples, but only 600 new samples were actually analyzed with the SSI-cov algorithm, demonstrating the filtering effect provided by the i-AOMA intelligent core based on the RF algorithm. Therefore, after collecting 600 new SDs, the convergence criterion based on Eq. (28) has been fulfilled. Figs. 6–8 illustrate the final results of the i-AOMA.

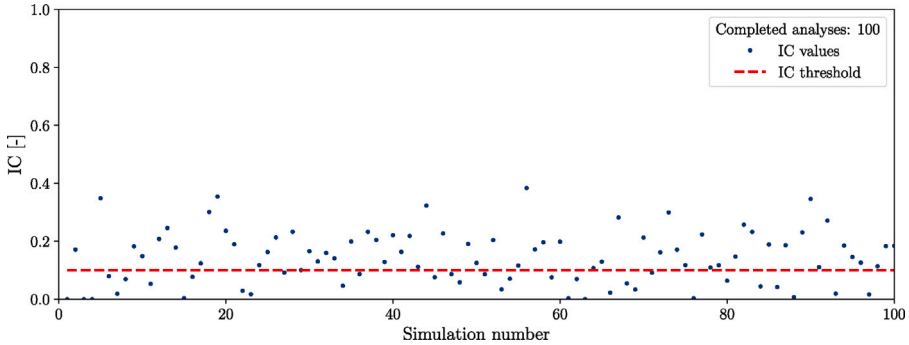

Fig. 5. Numerical benchmark case: numerical values of IC obtained from the sets of control parameters generated for training the intelligent core of i-AOMA.

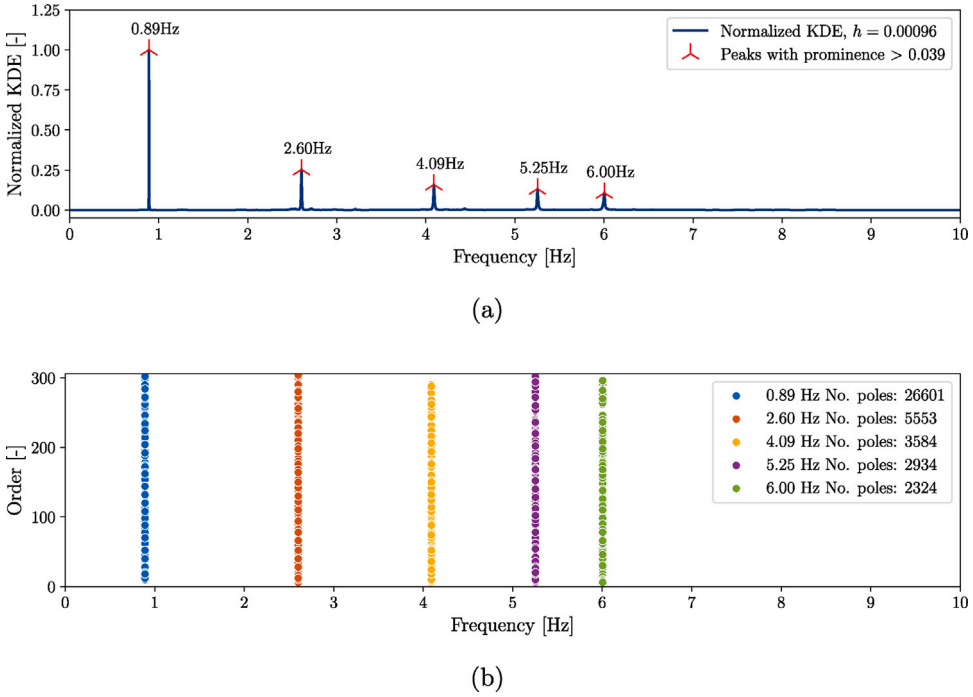

Fig. 6. Numerical benchmark case i-AOMA phase 2: the normalized KDE together with the identified peaks (a) and certainly stable poles falling within the retaining bands (b) obtained at the end of the i-AOMA.

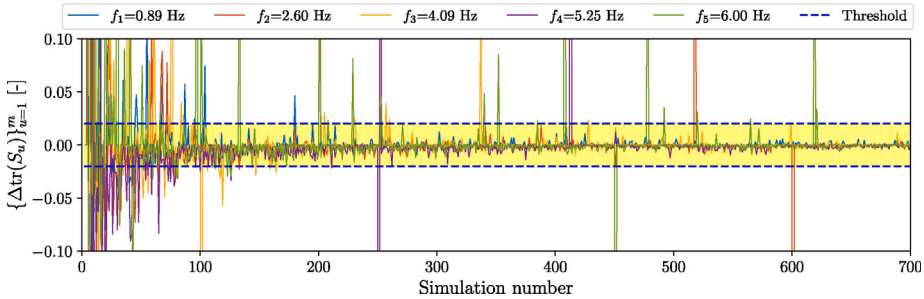

Fig. 7. Numerical benchmark case: convergence analysis of the relative total sample variance for each mode.

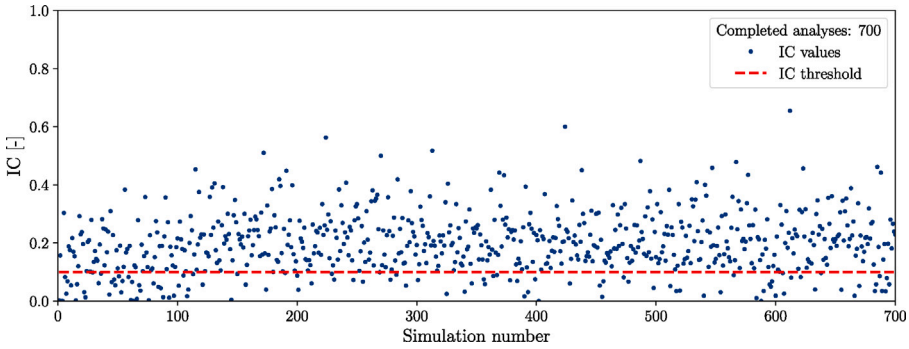

Fig. 8. Numerical benchmark case: numerical values of IC obtained from all the feasible sets of control parameters generated during i-AOMA.

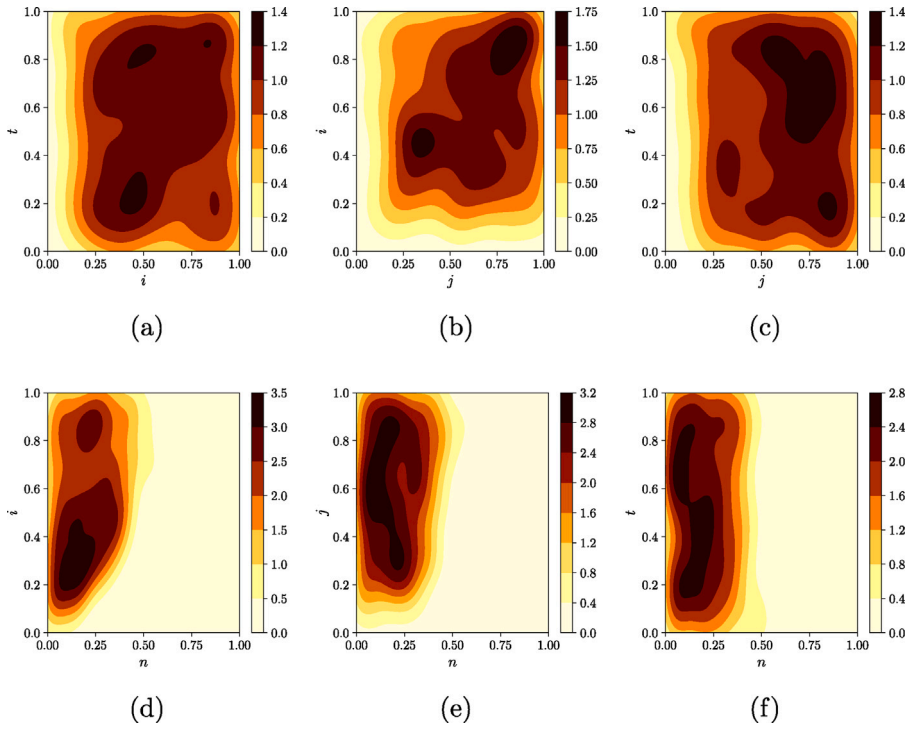

Fig. 9. Numerical benchmark case: joint probability density functions of the control parameters samples that have been classified as feasible from the intelligent core of i-AOMA.

It is worth noting in Fig. 6 that a lower estimate of the BW equal to 0.00096 Hz has been obtained with the ISJ algorithm. The reduction of the BW value in the i-AOMA phase 2 is due to the selection pressure provided by the RF algorithm, which reduces the uncertainty of the modal estimates attributable to the control parameters by driving the selection of their most appropriate values. Furthermore, Fig. 8 demonstrates that the trained RF algorithm drives intelligently the control parameters sampling, since most of the points are above the IC threshold value.

Fig. 9 illustrates the joint (bidimensional) probability density functions of the control parameters that have been classified as feasible from the intelligent core of i-AOMA. These plots provide interesting interpretative maps that illustrate where the best values of the control parameters were actually sampled for this benchmark case study.

The estimates of the natural frequencies for the present benchmark case are 0.89 Hz, 2.60 Hz, 4.09 Hz, 5.25 Hz, and 6.00 Hz. The corresponding estimates of the damping ratios are 1.97%, 1.99%, 2.12%, 2.13%, and 1.95%. The identified mode shapes are shown in Fig. 10. By resorting to a boxplot-type representation, this figure also highlights the uncertainty level related to the selected poles in Fig. 6, as it emerges from the corresponding combinations of the control parameters adopted for the SSI-cov algorithm.

Although the final stable poles are relatively close to each other, it is worth noting in Fig. 10 that the uncertainty due to the control parameter values propagates and possibly amplifies through the identification procedure. Notably, the uncertainty level in

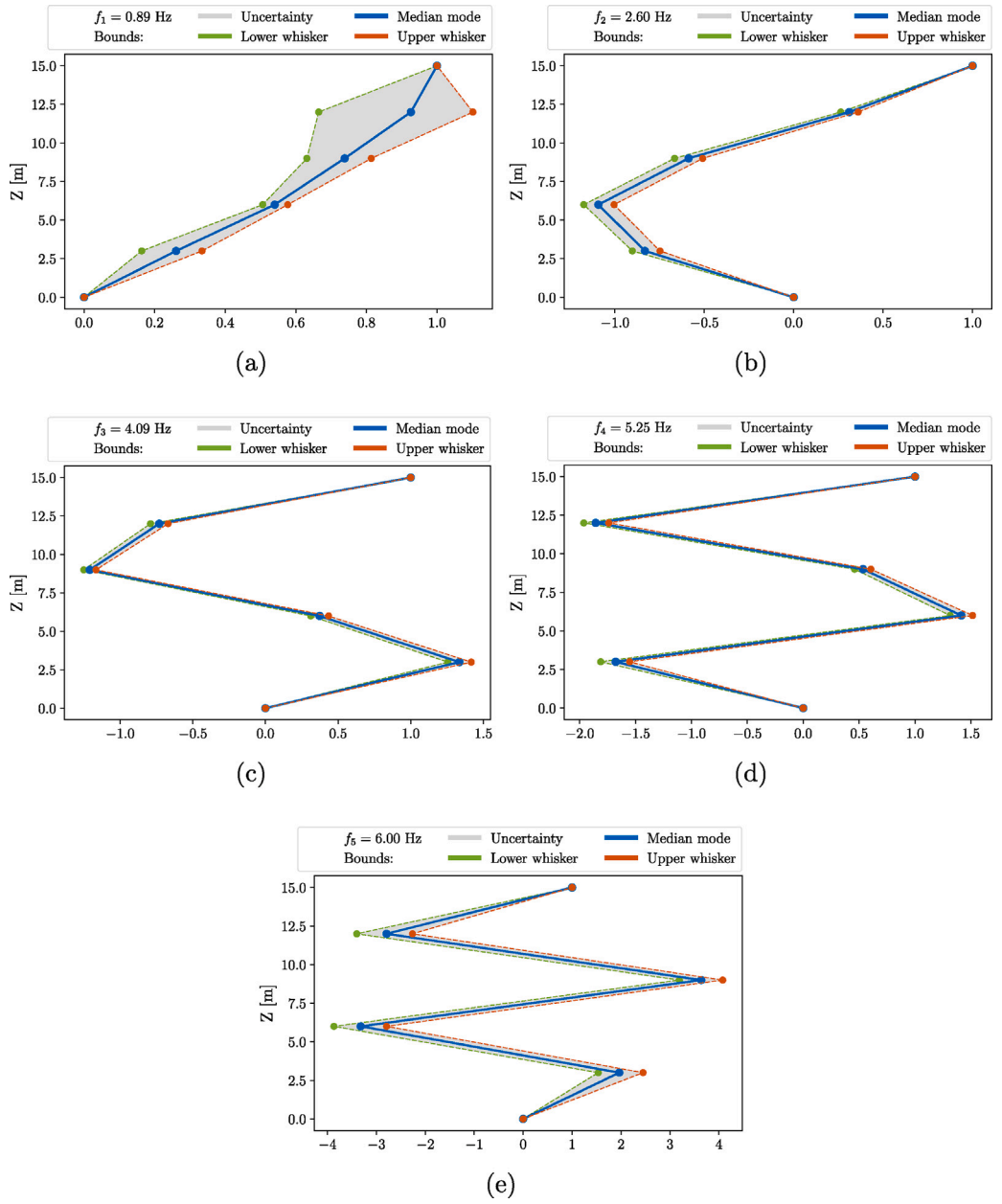

Fig. 10. Numerical benchmark case: median mode shapes and corresponding uncertainty level in terms of boxplot's whiskers.

the final mode shapes is not constant. On the contrary, it is very low in some cases but it can be also quite large, depending on the considered DOF and the mode number.

Eventually, Figs. 11–12 illustrate the convergence of average and standard deviation for natural frequencies and damping ratios, respectively, over all the feasible samples of the control parameters. The final standard deviation values in Figs. 11–12 show that the uncertainty level about the natural frequencies due to the variability of the control parameters is generally lower than that observed for the mode shapes. A significant uncertainty level is also observed for the estimation of the modal damping ratios.

It is pointed out that the original MC simulations-based construction of the SD has been applied for the sake of validation by considering all the quasi-random samples of the control parameters (i.e., without restricting the application of the SSI-cov algorithm to those control parameters that have been classified as feasible from the intelligent core of the i-AOMA). So doing, practically identical results have been obtained on average whereas narrow confidence bounds are obtained by means of the proposed i-AOMA. This is attributable to the selection pressure exerted by the RF algorithm, which allows reducing the uncertainties related to the

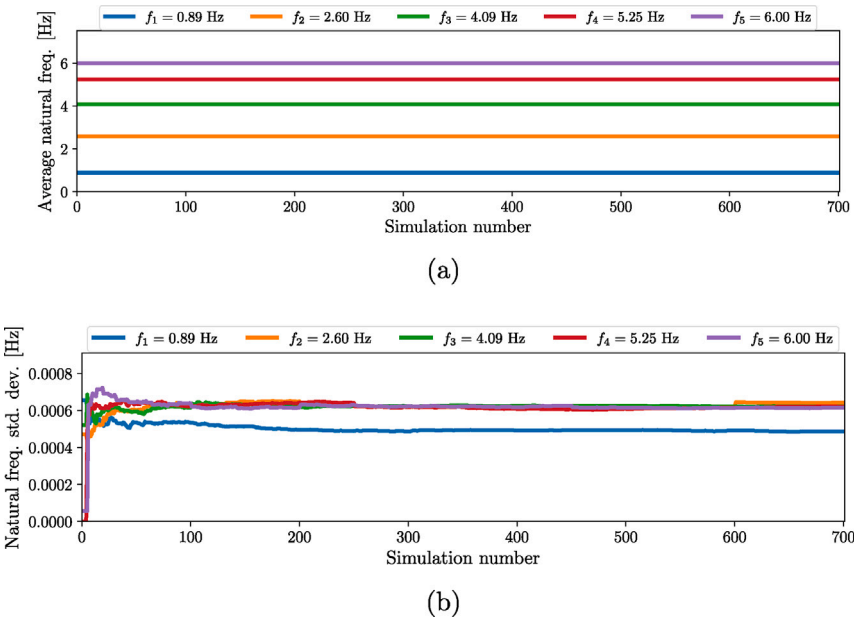

Fig. 11. Numerical benchmark case: average (a) and standard deviation (b) of natural frequencies over the feasible samples of the control parameters.

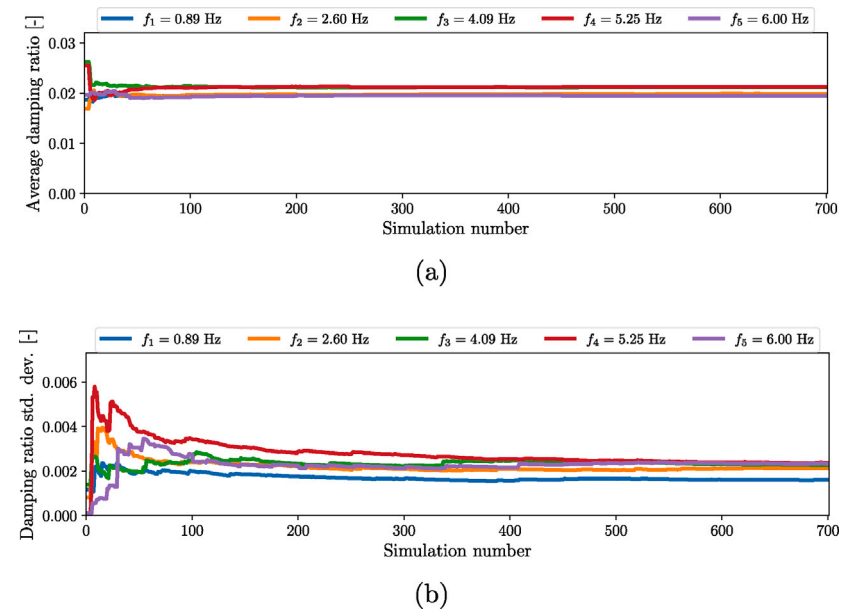

Fig. 12. Numerical benchmark case: average (a) and standard deviation (b) of damping ratios over the feasible samples of the control parameters.

variability of the control parameters. This demonstrates that the proposed i-AOMA methods allow for achieving more accurate results with no significant influence of the analyst's decisions while dramatically reducing the whole computational effort.

5. Case-study: identification of the Al-Hamra Firduos Tower

5.1. General description, sensor network for dynamic monitoring and finite element analysis

The proposed i-AOMA is finally applied to perform the modal identification of the Al-Hamra Firduos Tower (hereafter named Al-Hamra Tower for the sake of compactness), which is a sculptured skyscraper located in the center of Kuwait City, Kuwait.

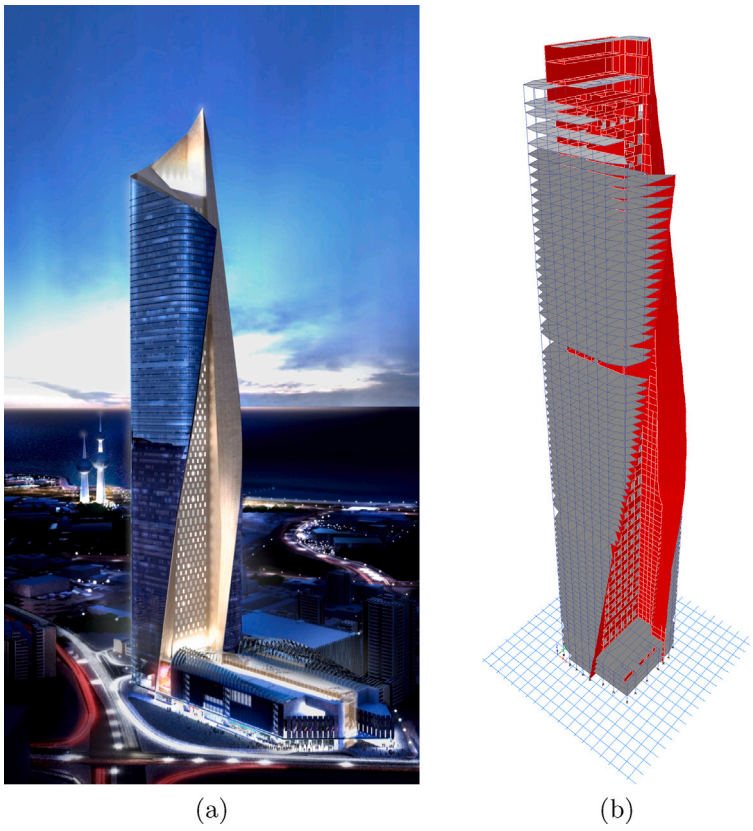

Fig. 13. Al-Hamra Tower: general view (a) and finite element model adopted for the modal analysis (b).

Started in 2005 and completed in 2011, this iconic high-rise building is composed of about 80 floors with a total height of 412.6 m, thus resulting the tallest building in Kuwait [60–62]. The skyscraper mainly hosts offices, whereas the first five floors are devoted to commercial uses. This commercial area extends beyond the planar footprint of the tower and merges with a multi-level car park area. However, this latter portion is structurally independent from the tower due to the presence of a decoupling expansion joint [60,61], and thus it is neglected in the current analysis.

From the architectural standpoint, the tower presents an approximately square sectional plan from the top view, with a removed slice on the southern edge and with an internal open void that creates a counter-clockwise facade twisting movement along the full height as shown in Fig. 13. The south-faced wall is made of concrete and has numerous openings with glass windows. East, west, and north-faced walls are made of glass curtain walls. Several technical challenges were faced during construction works, such as pumping concrete at high elevations. The concrete grade varies from C40 (toward top levels) to C70 (at low levels) [60]. The average inter-storey height is 4 m high, and the typical floor is entirely built with reinforced concrete beams and slabs.

From a structural standpoint, starting from the base, the Al-Hamra Tower is connected to the foundation level with a web-like concrete lamella structure visible at the lobby entrance level [60,61] in order to avoid buckling of the base columns. A 4 m depth raft foundation is placed above 289 cast-in-situ bored piles, which have a diameter equal to 1.2 m and extend up to 27 m inside the ground [61]. The high-rise building internal structural system relies on core shear walls with thicknesses varying between 1.20 m and 0.30 m along the height [61]. On the southern side of the building, perimeter curved shear walls provide further stability to the structural system [60]. Due to its twisting shape and thus variable floor plan shape, the center of mass shifts for each floor diaphragm along the height [60].

The Al-Hamra Tower was equipped with a sensor network consisting of 24 biaxial force balance accelerometers to record its horizontal dynamic response in the north and east directions, which are labeled as X and Y directions, respectively, as illustrated in Fig. 14. Particularly, Fig. 14 shows that the typical instrumented floor is monitored by means of three accelerometers placed at three extreme corners, so as to capture the torsional motion of the tower. The full-scale range of the accelerometers is ±4 g, the dynamic range is larger than 155 dB (DC to 10 Hz), and the sensitivity is 2.5 V/g.

The sensors' position is detailed in Table 1. It is worth noting that the sensors at the B2 floor are actually located at slightly different elevations due to technical installation reasons [60]. However, the elevation change within the B2 level compared to the elevation variations between the monitored floors is negligible. All the sensors are connected to the data loggers by means of cables. The multi-channel centralized data loggers are installed in the refuge area located on the 54th floor. The sensors are synchronized by a GPS installed on the top of the roof.

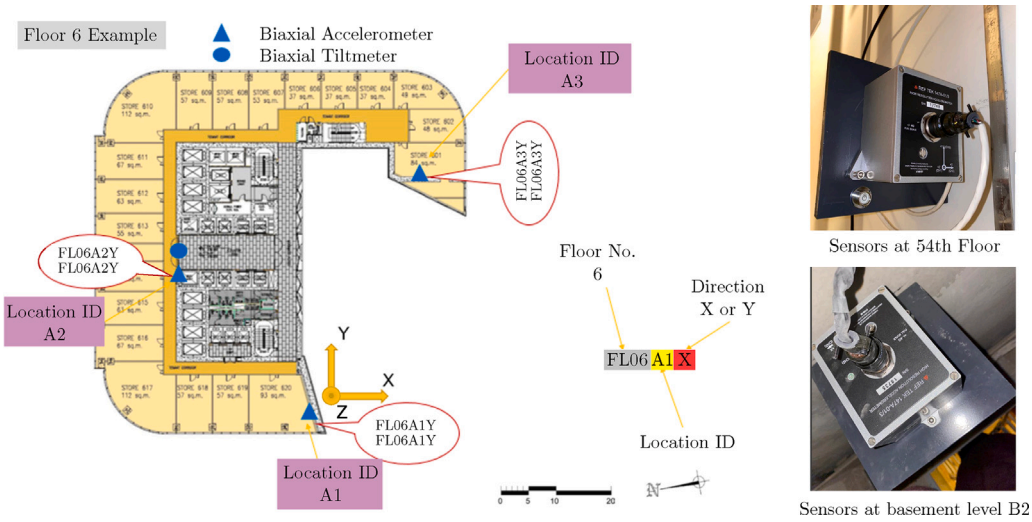

Fig. 14. Al-Hamra Tower: typical monitored floor of the Al-Hamra Tower (left) and view of the biaxial accelerometers (right).

Table 1
Al-Hamra Tower: location of the accelerometers.

Sensor ID	X [mm]	Y [mm]	Z [mm]	Floor number
FL76A1	15,150	1,320		
FL76A2	−700	19,935	344000	76
FL76A3	15,150	34,050		
FL65A1	7,955	−600		
FL65A2	−700	12,835	295075	65
FL65A3	16,295	35,300		
FL54A1	40,475	2,645		
FL54A2	−800	20,975	246602	54
FL54A3	16,525	46,125		
FL42A1	15,450	−800		
FL42A2	−900	14,235	194375	42
FL42A3	20,390	35,250		
FL29A1	36,018	−9,247		
FL29A2	−900	14,575	137360	29
FL29A3	32,332	35,360		
FL16A1	15,385	−800		
FL16A2	−900	13,865	80975	16
FL16A3	29,685	35,350		
FL06A1	22,235	−11,870		
FL06A2	−900	13,775	38975	6
FL06A3	38,600	29,675		
FLB2A1	45,100	−12,050	−4400	
FLB2A2	−1,200	14,200	−6220	B2
FLB2A3	35,285	45,480	−7090	

Modal properties of the tower have been preliminarily obtained from the high-fidelity finite element model [60] illustrated in Fig. 13. Details about the finite element model of the tower can be found in the paper by Sun et al. [60]. Numerical results of the modal analysis for the first 15 modes are reported in Table 2. It is evident from Table 2 that the first 15 modes mobilize almost the entire cumulative mass participating ratio (about 90%), except for the rotational mass in X and Y directions (about 82%). The first five modes are characterized by very close natural frequencies and are lower than 1 Hz.

5.2. Identification under ambient vibrations

The experimental data for the present application were collected from the sensor network on May 2, 2022. One-hour monitoring data with a sampling frequency $f_s = 200$ Hz are analyzed. The monitored data were decimated with a factor equal to 40 in order to investigate accurately the low frequency modes of the structure. According to the Nyquist's theorem, the upper bound of the observable frequency range is thus equal to 2.50 Hz. Fig. 15 illustrates the time-histories of the recorded accelerations at three

Table 2
Al-Hamra Tower: numerical values of the modal properties estimated from finite element analysis (T is the natural period; f is the natural frequency; UX and UY represent the participating mass ratio along X direction and Y direction, respectively; RX, RY and RZ denote the participating rotational mass ratio along X direction, Y direction and vertical direction, respectively; the symbol Σ stands for cumulative sum of the participating mass ratios up to that mode number).

Mode	T [s]	f [Hz]	UX [–]	UY [–]	RX [–]	RY [–]	RZ [–]
1	6.441	0.155	0.467	0.152	0.091	0.285	0.020
2	4.705	0.213	0.141	0.483	0.280	0.101	3.54E−05
3	2.761	0.362	0.009	0.004	2.00E−04	0.002	0.686
4	1.459	0.685	0.173	0.003	0.016	0.199	0.001
5	1.178	0.849	0.010	0.156	0.217	0.009	6.00E−04
6	0.938	1.066	0.001	8.00E−04	0.003	4.00E−04	0.114
7	0.692	1.446	0.062	0.003	0.002	0.097	1.00E−04
8	0.559	1.789	0.003	0.004	0.006	0.005	0.047
9	0.535	1.870	0.002	0.054	0.082	0.005	0.003
10	0.399	2.509	0.038	0.001	0.002	0.076	2.00E−04
11	0.355	2.814	2.00E−04	2.53E−05	1.00E−04	3.00E−04	0.035
12	0.33	3.026	0.001	0.036	0.067	0.003	2.95E−05
13	0.264	3.784	0.018	3.00E−04	4.00E−04	0.040	0.003
14	0.256	3.911	0.004	1.00E−04	1.00E−04	0.009	0.023
15	0.228	4.392	1.08E−05	0.028	0.055	1.61E−05	1.00E−04
Mode	T [s]	f [Hz]	ΣUX [–]	ΣUY [–]	ΣRX [–]	ΣRY [–]	ΣRZ [–]
1	6.441	0.155	0.467	0.152	0.091	0.285	0.020
2	4.705	0.213	0.609	0.634	0.370	0.385	0.020
3	2.761	0.362	0.617	0.639	0.370	0.388	0.706
4	1.459	0.685	0.791	0.642	0.386	0.586	0.707
5	1.178	0.849	0.800	0.798	0.603	0.595	0.708
6	0.938	1.066	0.802	0.799	0.606	0.596	0.821
7	0.692	1.446	0.864	0.802	0.608	0.693	0.821
8	0.559	1.789	0.867	0.806	0.614	0.698	0.868
9	0.535	1.870	0.869	0.860	0.695	0.702	0.871
10	0.399	2.509	0.907	0.861	0.698	0.778	0.871
11	0.355	2.814	0.908	0.861	0.698	0.778	0.905
12	0.33	3.026	0.909	0.897	0.765	0.781	0.905
13	0.264	3.784	0.927	0.898	0.765	0.820	0.908
14	0.256	3.911	0.931	0.898	0.765	0.829	0.931
15	0.228	4.392	0.931	0.925	0.820	0.829	0.931

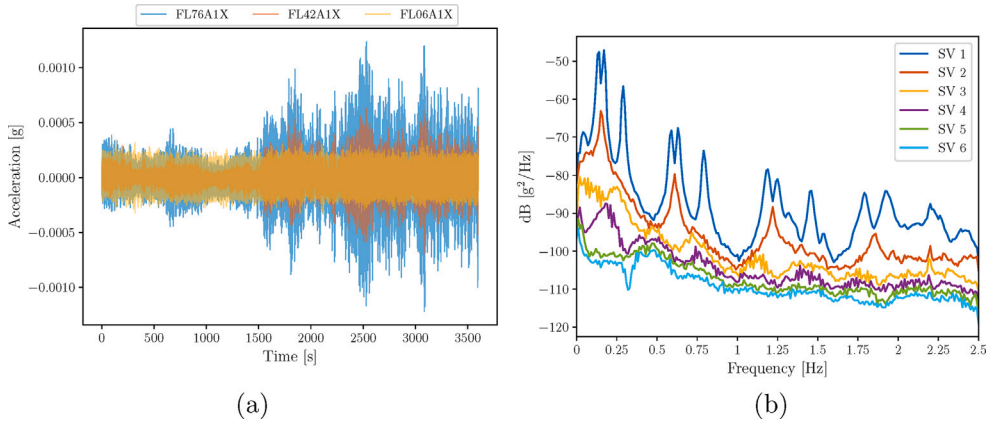

Fig. 15. Al-Hamra Tower: accelerations recorded on May 2, 2022 at 6th, 42th, and 76th floor (a) and singular value decomposition of the power spectral density limited to the first six singular values (b).

different floors and the singular value decomposition of the power spectral density limited to the first six higher singular values. The Welch's method has been adopted by setting the Hann window length and the overlap percentage equal to 500 points and 50%, respectively [63]. Furthermore, the stationarity of the recorded dynamic responses have been verified through the augmented Dickey–Fuller test [64,65].

The inspection of the singular value decomposition of the power spectral density shows that $f_f = 0.16$ Hz. Hence, the bounds of the control parameters are roughly defined according to Eqs. (12)–(15). The number of quasi-random samples of the control parameters generated by means of the Halton technique for the present case study is set to $s = 200$. Specifically, 631 applications of the SSI-cov algorithm out of 831 total generated samples have not been completed because of numerical failure or excessive

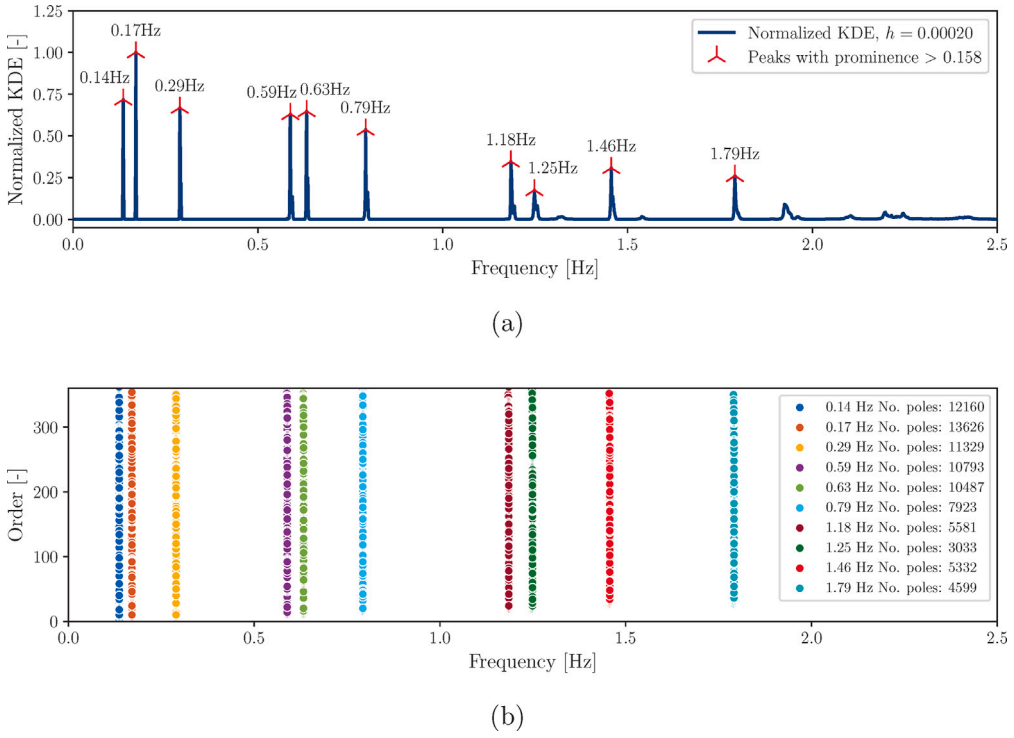

Fig. 16. Al-Hamra Tower: normalized KDE together with the identified peaks (a) and certainly stable poles falling within the retaining bands (b) obtained from the sets of control parameters generated for training the intelligent core of i-AOMA.

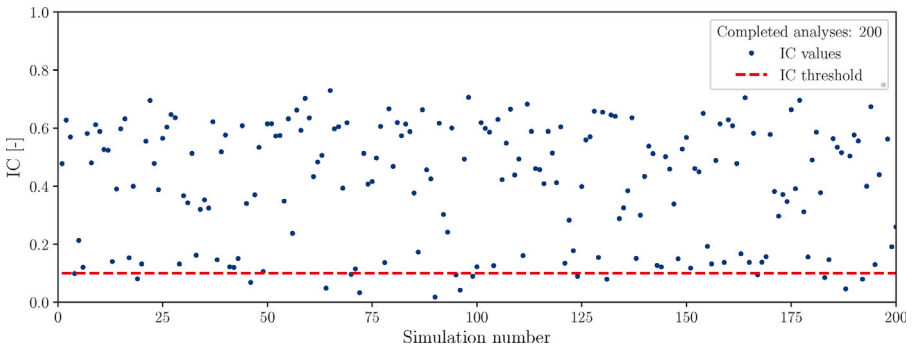

Fig. 17. Al-Hamra Tower: numerical values of IC obtained from the sets of control parameters generated for training the intelligent core of i-AOMA.

elaboration time (success rate about 24%). Once the SDs corresponding to $s = 200$ successful applications of the SSI-cov algorithm have been overlapped, stability checks have been performed according to Eqs. (16)–(19) and possibly stable poles are then identified. The FFT-KDE algorithm has been next performed considering these possibly stable poles. So doing, an estimate of the BW equal to 0.0002 Hz is obtained by means of the ISJ algorithm. The statistical value of the prominence threshold for the peaks' identification from the normalized KDE (99th percentile in the fitted Beta distribution) is equal to 0.1585, and $b_w = 3$ has been calculated. Next, the database consisting of all the generated control parameters and the corresponding IC values is prepared in order to train the RF algorithm. Figs. 16–17 illustrate the main results obtained from the $s = 200$ sets of control parameters generated for training the intelligent core of i-AOMA.

Afterward, new quasi-random samples of the control parameters are generated by means of the Halton technique and the SSI-cov algorithm is performed only for those that are classified as feasible. The convergence criterion based on Eq. (28) has been fulfilled when the trained RF algorithm has enabled the application of the SSI-cov algorithm for 500 newly samples out of 2311 quasi-random combinations of the control parameters. Figs. 18–20 illustrate the final results of the i-AOMA.

It is noted in Fig. 18 that the ISJ algorithm now provides an estimate of the BW equal to 0.00016 Hz whereas it results in $b_w = 4$. Therefore, the BW has reduced while b_w increased. Once again, therefore, the selection pressure provided by the RF algorithm has reduced the dispersion of the final certainly stable poles, thereby lowering the uncertainty level about the modal estimates

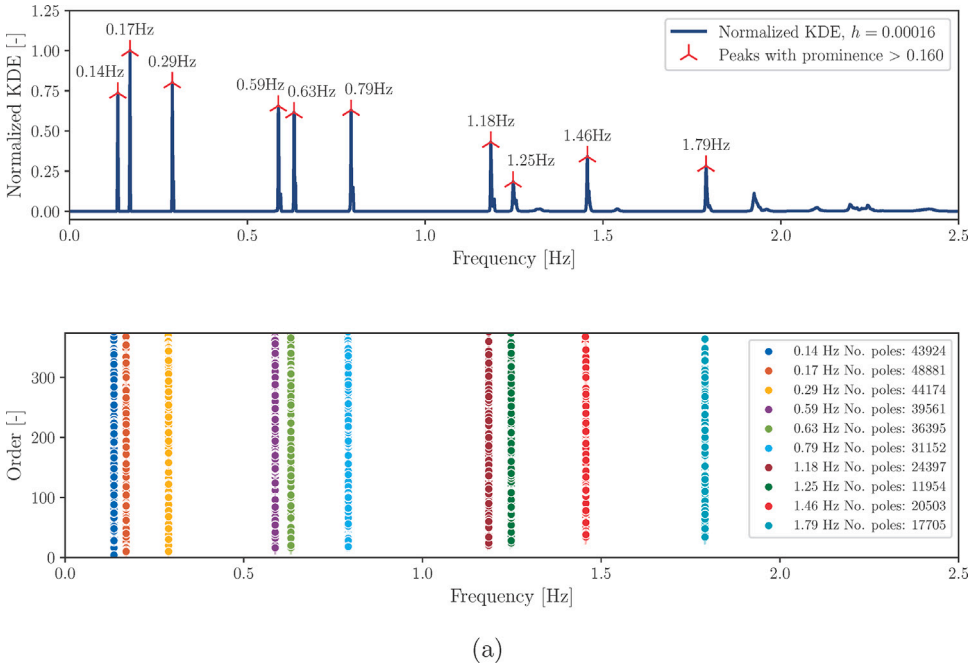

(a)

Fig. 18. Al-Hamra Tower: the normalized KDE together with the identified peaks (a) and certainly stable poles falling within the retaining bands (b) obtained at the end of the i-AOMA.

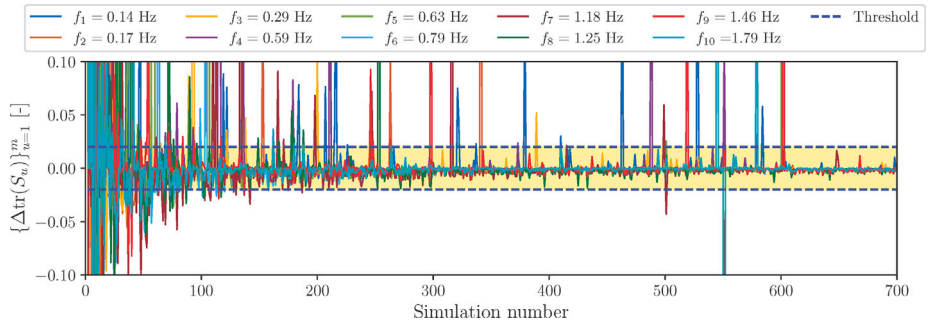

Fig. 19. Al-Hamra Tower: convergence analysis of the relative total sample variance for each mode.

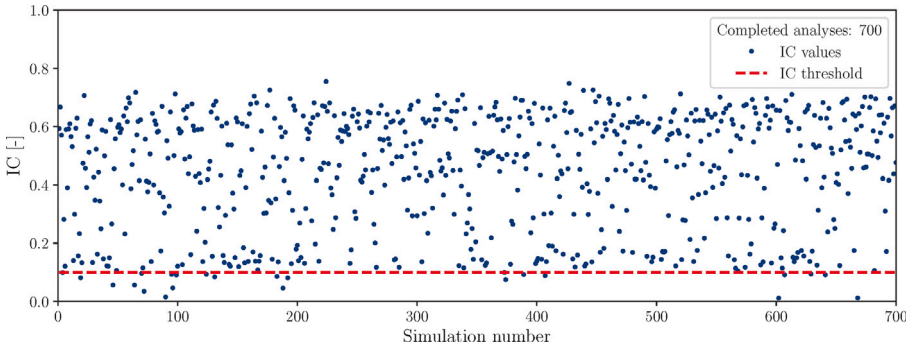

Fig. 20. Al-Hamra Tower: numerical values of IC obtained from all the feasible sets of control parameters generated during i-AOMA.

attributable to the control parameters. Moreover, Fig. 20 confirms the effectiveness of the trained RF algorithm in selecting feasible sets of control parameters for modal identification, given the small number of events for which the IC value is lower than the threshold.

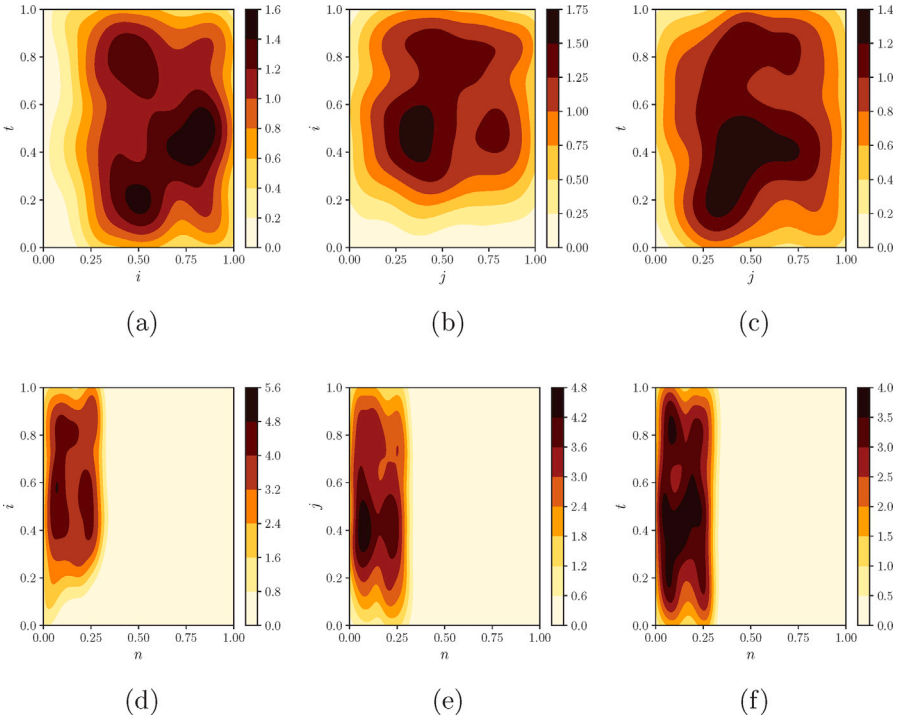

Fig. 21. Al-Hamra Tower: joint probability density functions of the control parameters that have been classified as feasible from the intelligent core of i-AOMA.

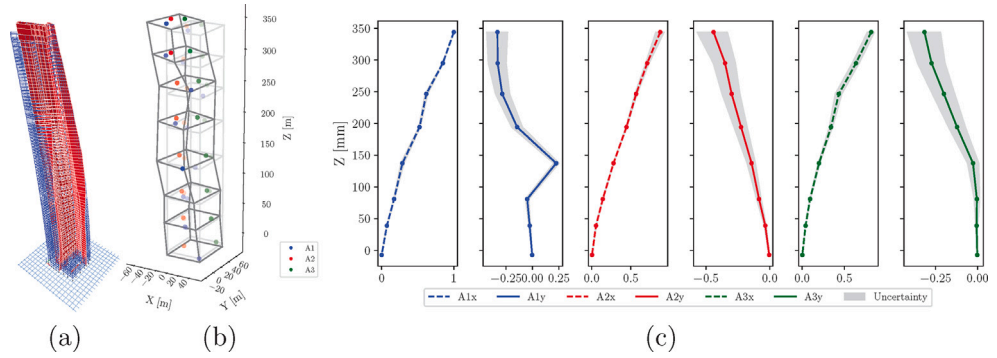

Fig. 22. Al-Hamra Tower: numerical mode shape (a), median experimental mode shape (b) and corresponding uncertainty level in terms of boxplot's whiskers (c) for the first mode of the tower.

Fig. 21 illustrates the joint (bidimesional) probability density functions of the control parameters that have been classified as feasible from the intelligent core of i-AOMA. The comparison between Figs. 21 and 9 demonstrates, as expected, that the most appropriate combinations of the control parameters of the SSI-cov algorithm change on a case-by-case basis. This, in turn, confirms the need for an automatic procedure for their optimal tuning.

Ten modes of the tower have been identified corresponding to natural frequencies value equal to 0.14 Hz, 0.17 Hz, 0.29 Hz, 0.59 Hz, 0.63 Hz, 0.79 Hz, 1.18 Hz, 1.25 Hz, 1.46 Hz, and 1.79 Hz. The related estimates of the damping ratios are 1.08%, 0.54%, 0.66%, 0.76%, 0.58%, 0.62%, 0.82%, 1.11%, 0.75%, and 1.05%. The corresponding mode shapes are shown in Figs. 22–31, which are plotted considering a simplified wireframe geometrical model derived from the sensor network layout. The uncertainty level of the mode shapes due to the variability of the control parameters adopted for the SSI-cov algorithm is highlighted by means of a boxplot-type representation. Numerical mode shapes obtained from the finite element analysis are also shown in Figs. 22–31.

A satisfactory matching can be observed between the estimated mode shapes and the corresponding numerical predictions. The first eight modes are also in very good agreement with previous experimental results reported by Sun et al. [60]. The last two modes shapes identified in the present study were never detected before, and they are in good agreement with numerical predictions obtained from the finite element model (modes number 9 and 10 in Table 2). Table 3 provides a synthetic comparative assessment between the results reported by Sun et al. [60] and those obtained in the present study.

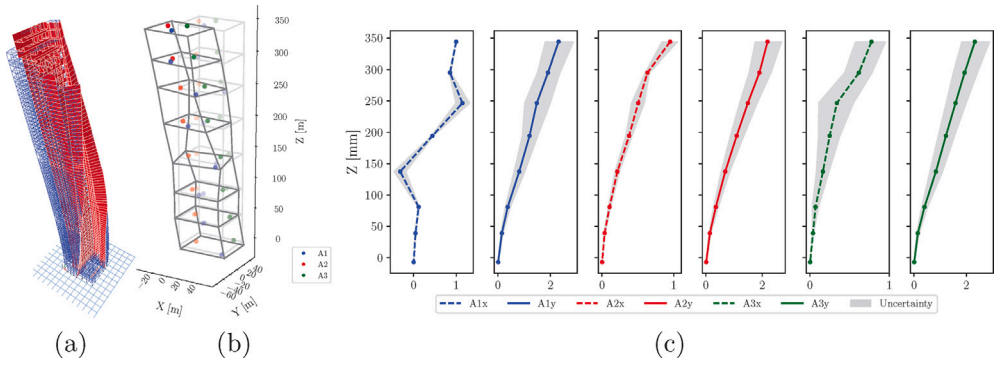

Fig. 23. Al-Hamra Tower: numerical mode shape (a), median experimental mode shape (b) and corresponding uncertainty level in terms of boxplot's whiskers (c) for the second mode of the tower.

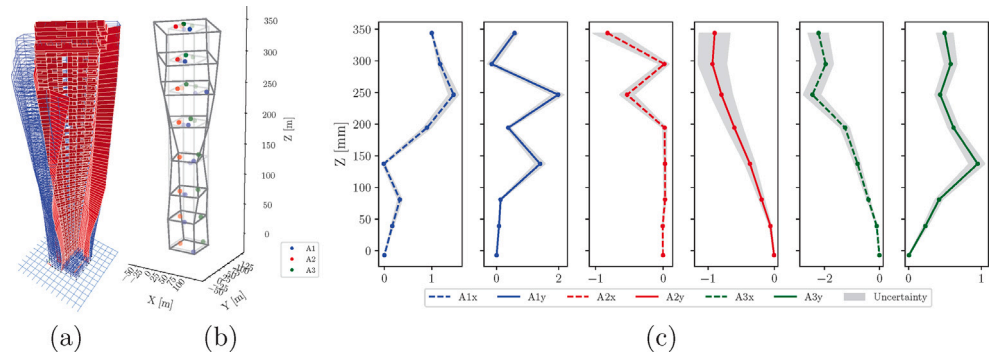

Fig. 24. Al-Hamra Tower: numerical mode shape (a), median experimental mode shape (b) and corresponding uncertainty level in terms of boxplot's whiskers (c) for the third mode of the tower.

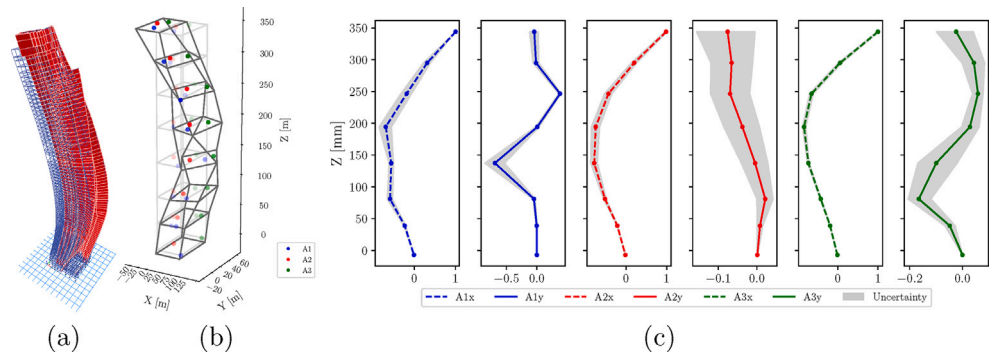

Fig. 25. Al-Hamra Tower: numerical mode shape (a), median experimental mode shape (b) and corresponding uncertainty level in terms of boxplot's whiskers (c) for the fourth mode of the tower.

Once again, it is evident from Figs. 22–31 that the uncertainty due to the control parameter values propagates and possibly amplify through the identification procedure, even if the final stable poles are relatively close each other. It is also confirmed that the uncertainty level is not constant. While it is very low in some cases, it results very large in others. The uncertainty level depends on which DOF and mode number is considered, and, as expected, higher modes are often associated with a higher uncertainty.

Finally, the convergence of average and standard deviation for natural frequencies and damping ratios over all the feasible samples of the control parameters are reported in Figs. 32–33, respectively.

6. Conclusions

This work was meant at contributing to current efforts towards the fully automation of the algorithms for structural identification.

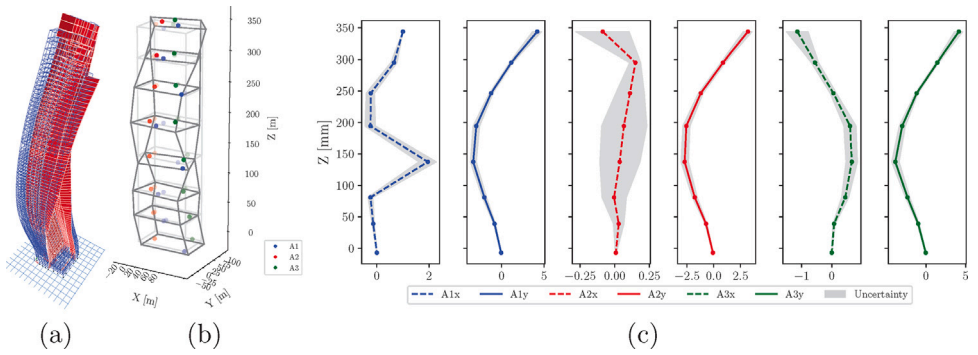

Fig. 26. Al-Hamra Tower: numerical mode shape (a), median experimental mode shape (b) and corresponding uncertainty level in terms of boxplot's whiskers (c) for the fifth mode of the tower.

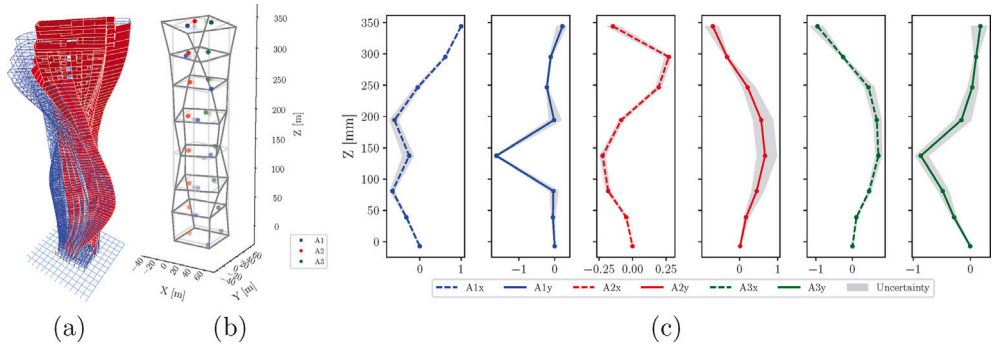

Fig. 27. Al-Hamra Tower: numerical mode shape (a), median experimental mode shape (b) and corresponding uncertainty level in terms of boxplot's whiskers (c) for the sixth mode of the tower.

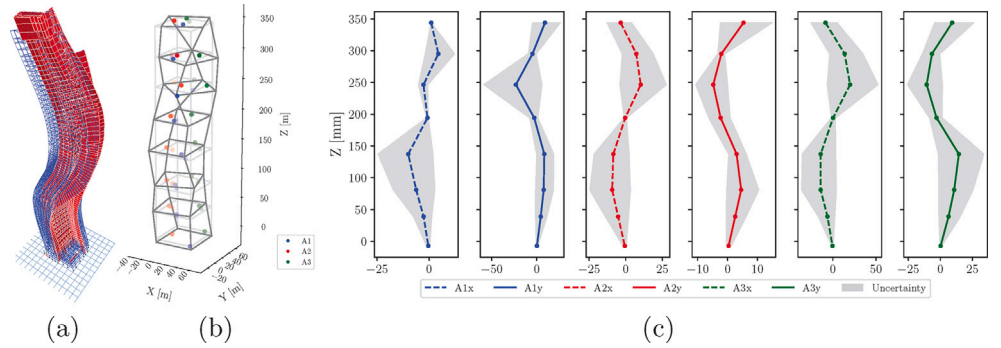

Fig. 28. Al-Hamra Tower: numerical mode shape (a), median experimental mode shape (b) and corresponding uncertainty level in terms of boxplot's whiskers (c) for the seventh mode of the tower.

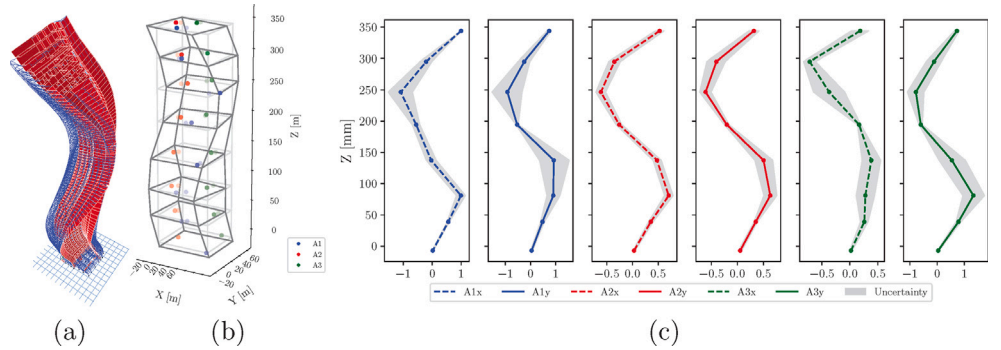

Fig. 29. Al-Hamra Tower: numerical mode shape (a), median experimental mode shape (b) and corresponding uncertainty level in terms of boxplot's whiskers (c) for the eighth mode of the tower.

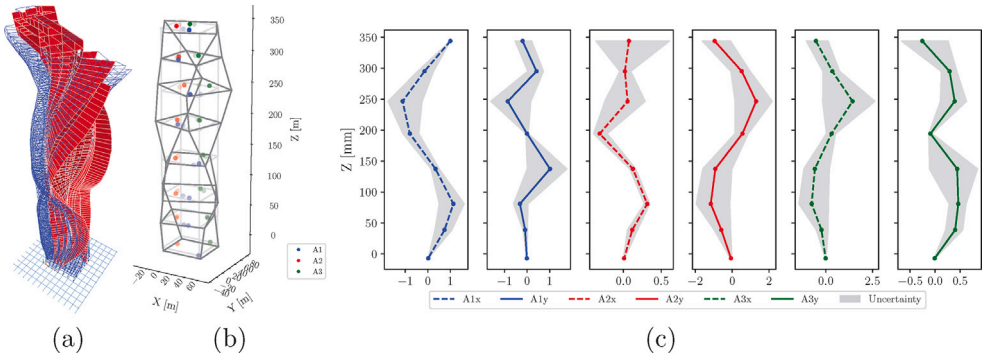

Fig. 30. Al-Hamra Tower: numerical mode shape (a), median experimental mode shape (b) and corresponding uncertainty level in terms of boxplot's whiskers (c) for the ninth mode of the tower.

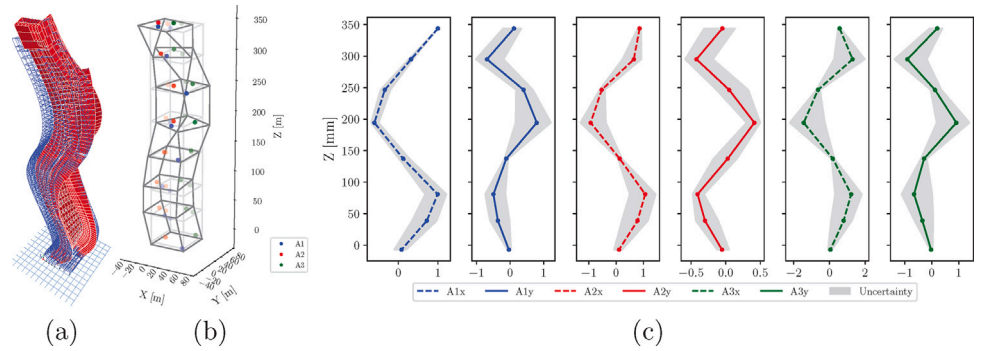

Fig. 31. Al-Hamra Tower: numerical mode shape (a), median experimental mode shape (b) and corresponding uncertainty level in terms of boxplot's whiskers (c) for the tenth mode of the tower.

Table 3
Al-Hamra Tower: comparison between the results reported by Sun et al. [60] and those obtained in the present study by means of the i-AOMA algorithm (f is the natural frequency, whereas ξ indicates the damping ratio).

Mode No.	Mode type	Sun et al. [60]	This study	
		f [Hz]	f [Hz]	ξ [%]
1	NS flexural (1)	0.14	0.14	1.08
2	EW flexural (1)	0.18	0.17	0.54
3	Torsional (1)	0.31	0.29	0.66
4	NS flexural (2)	0.61	0.59	0.76
5	EW flexural (2)	0.66	0.63	0.58
6	Torsional (2)	0.84	0.79	0.62
7	NS flexural (3)	1.24	1.18	0.82
8	EW flexural (3)	1.30	1.25	1.11
9	Torsional (3)	–	1.46	0.75
10	NS flexural (4)	–	1.79	1.05

To this end, a computational framework for the intelligent automatic operational modal analysis (i-AOMA) of linear structures under ambient vibrations has been proposed. It exploits the covariance-based stochastic subspace (SSI-cov) algorithm for the output-only identification of the modal parameters and the overall workflow consists of two main phases. The first phase provides a database for training the intelligent random forest (RF) core based on the identification results in terms of stabilization diagrams (SD) by randomly varying the control parameters of the SSI-cov. In the second phase, the quasi-random sampling of new sets of control parameters is intelligently driven by the RF until a statistical convergence criterion is reached. Final stable modal results of interest are then extracted from the stabilization diagrams and relevant statistics are computed to evaluate the uncertainty level attributable to the control parameters of the SSI-cov algorithm. The proposed i-AOMA has been applied to estimate the modal parameters of the Al-Hamra Firduos Tower located in Kuwait City. The entire Python source code of i-AOMA is made freely available along with the present work.

It is worth remarking that the proposed method relies on the standard SSI-cov technique, from which it inherits all its main characteristics, including the robustness against the noise [66–68]. Indeed, this study aims at enabling its reliable automatic

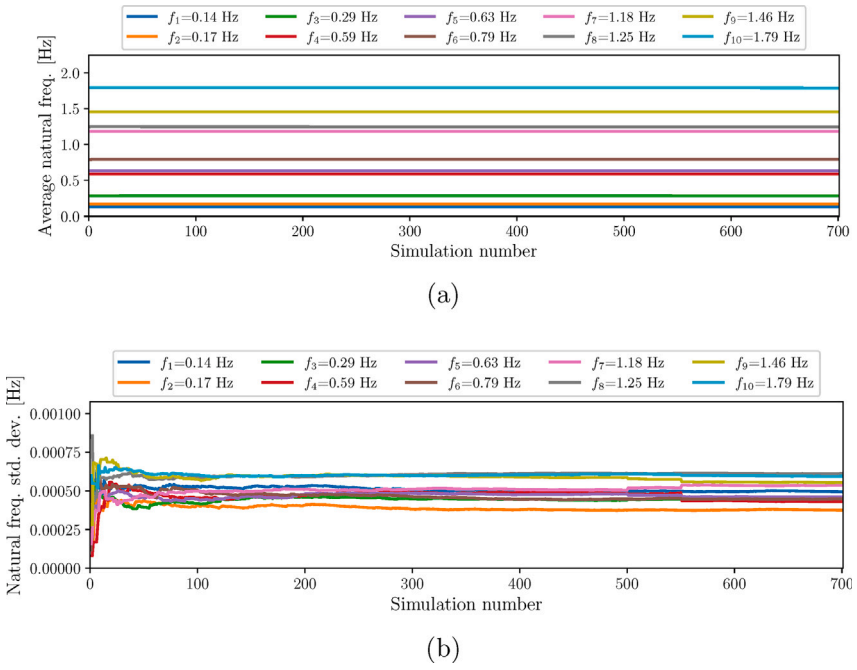

Fig. 32. Al-Hamra Tower: average (a) and standard deviation (b) of natural frequencies over the feasible samples of the control parameters.

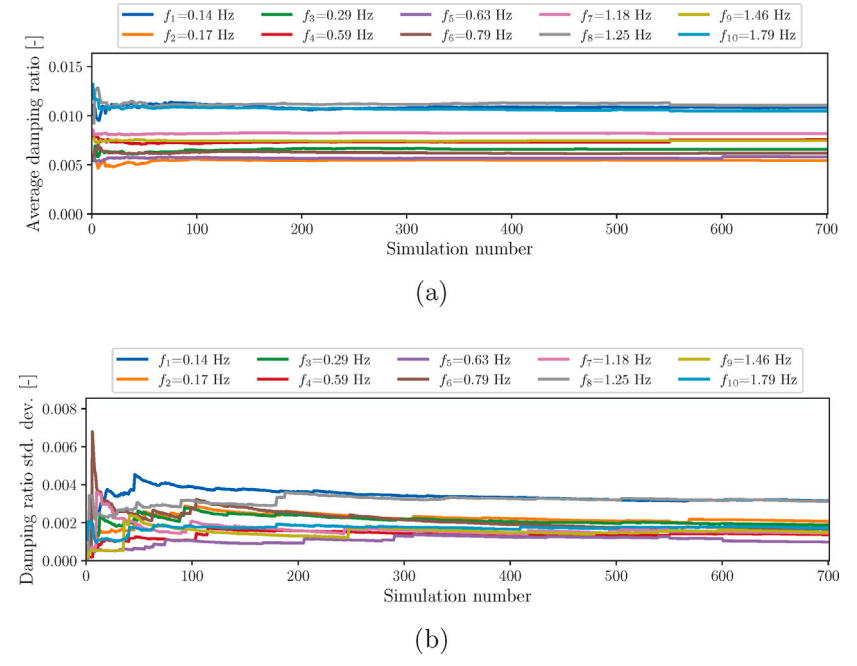

Fig. 33. Al-Hamra Tower: average (a) and standard deviation (b) of damping ratios over the feasible samples of the control parameters.

implementation by means of an original computational framework that implements novel solutions to achieve two goals. The foremost objective is the automatic calibration of the control parameters, which has been pursued through a suitable computational intelligence algorithm. Ultimately, the overall algorithm no longer depends on the analyst's decisions about the involved control parameters, while only a few general settings are required. The second objective is a clear evaluation of the effects of the uncertainty about the control parameters. Hence, a rational methodology has been developed to quantify how the uncertainty about the control parameters propagates into the final modal estimates. So doing, the uncertainty level affecting the final modal estimates due to the

variability of the control parameters is always made explicit. The main limitation of the proposed i-AOMA method is attributable to the total computational effort. Although the elaboration time has been mitigated by exploiting an efficient object-oriented programming approach and can be further reduced through a suitable parallelization, it is beyond doubt that the computational effort is much higher than other existing proposals for AOMA.

It is noteworthy that the proposed strategy can be adapted to accommodate other identification algorithms. This paves the way to further versions of the proposed approach, for example targeted at identifying structural systems from nonstationary time histories or in case of nonlinear behaviors. Possible improvements of the proposed computational framework include the implementation a Bayesian approach to deal with the uncertainties due to the control parameters.

Declaration of competing interest

The authors declare that they have no known competing financial interests or personal relationships that could have appeared to influence the work reported in this paper.

Data availability

The Python developed code is freely accessible from dedicated repository. Due to legal questions, raw monitoring data from the Al-Hamra Firduos Tower would remain confidential and would not be shared.

Acknowledgments

The authors thank the Kuwait Institute for Scientific Research and Jamal Al-Qazweeni for providing the ambient vibration data of the Al-Hamra Tower, which have been shared by Jafarali Parol.

Giuseppe Carlo Marano and Marco Martino Rosso acknowledge the support from PNRR MUR project PE0000013-FAIR (National Recovery and Resilience Plan – NRRP, Mission 4, Component 2, Investment 1.3, NextGenerationEU – D.D. 341 15/3/2022 and D.D. 1555 11/10/2022, PE0000013).

The work of Giuseppe Quaranta is partially framed within the RETURN Extended Partnership funded by the European Union Next-GenerationEU (National Recovery and Resilience Plan – NRRP, Mission 4, Component 2, Investment 1.3 – D.D. 1243 2/8/2022, PE0000005).

Open access funding provided by Politecnico di Torino within the CRUI-CARE Agreement.

Supplementary material statement

The code implemented in the present work is made freely available at the following Google Colab notebook link: https://colab.research.google.com/drive/1D6z1zM7lqJavI6yyMCI8BMnEqV9zw7kW?usp=sharing. It is also freely available at the following GitHub repository: https://github.com/marco-rosso-m/i-AOMA.

References

[1] F. Magalhães, Á. Cunha, E. Caetano, Vibration based structural health monitoring of an arch bridge: From automated OMA to damage detection, Mech. Syst. Signal Process. 28 (2012) 212–228.
[2] M. Mazzeo, D. De Domenico, G. Quaranta, R. Santoro, Automatic modal identification of bridges based on free vibration response and variational mode decomposition technique, Eng. Struct. 280 (2023) 115665.
[3] C. Rainieri, G. Fabbrocino, Operational Modal Analysis of Civil Engineering Structures, Vol. 142, Springer, New York, 2014, p. 143.
[4] D.P. Pasca, A. Aloisio, M.M. Rosso, S. Sotiropoulos, PyOMA and PyOMA_GUI: A Python module and software for operational modal analysis, SoftwareX 20 (2022) 101216.
[5] E.P. Carden, J.M. Brownjohn, Fuzzy clustering of stability diagrams for vibration-based structural health monitoring, Comput.-Aided Civ. Infrastruct. Eng. 23 (5) (2008) 360–372.
[6] F. Magalhaes, A. Cunha, E. Caetano, Online automatic identification of the modal parameters of a long span arch bridge, Mech. Syst. Signal Process. 23 (2) (2009) 316–329, http://dx.doi.org/10.1016/j.ymssp.2008.05.003, cited By 365.
[7] E. Reynders, J. Houbrechts, G. De Roeck, Fully automated (operational) modal analysis, Mech. Syst. Signal Process. 29 (2012) 228–250, http://dx.doi.org/10.1016/j.ymssp.2012.01.007, cited By 311.
[8] A. Cabboi, F. Magalhaes, C. Gentile, A. Cunha, Automated modal identification and tracking: Application to an iron arch bridge, Struct. Control Health Monit. 24 (1) (2017) http://dx.doi.org/10.1002/stc.1854, cited By 113.
[9] M. He, P. Liang, J. Li, Y. Zhang, Y. Liu, Fully automated precise operational modal identification, Eng. Struct. 234 (2021) 111988.
[10] M. He, P. Liang, E. OBrien, X. Sun, Y. Zhang, Continuous modal identification and tracking of a long-span suspension bridge using a robust mixed-clustering method, J. Bridge Eng. 27 (3) (2021) 05022001.
[11] G. Zini, M. Betti, G. Bartoli, A quality-based automated procedure for operational modal analysis, Mech. Syst. Signal Process. 164 (2022) 108173.
[12] Y. He, J.P. Yang, X.-F. Li, A three-stage automated modal identification framework for bridge parameters based on frequency uncertainty and density clustering, Eng. Struct. 255 (2022) 113891.
[13] Q.-M. Zhong, S.-Z. Chen, Z. Sun, L.-C. Tian, Fully automatic operational modal analysis method based on statistical rule enhanced adaptive clustering method, Eng. Struct. 274 (2023) 115216.
[14] F. Ubertini, C. Gentile, A. Materazzi, Automated modal identification in operational conditions and its application to bridges, Eng. Struct. 46 (2013) 264–278, http://dx.doi.org/10.1016/j.engstruct.2012.07.031, cited By 190.
[15] R. Cardoso, A. Cury, F. Barbosa, A robust methodology for modal parameters estimation applied to SHM, Mech. Syst. Signal Process. 95 (2017) 24–41, http://dx.doi.org/10.1016/j.ymssp.2017.03.021, cited By 44.

[16] R. de Almeida Cardoso, A. Cury, F. Barbosa, A clustering-based strategy for automated structural modal identification, Struct. Health Monit. 17 (2) (2018) 201–217.
[17] J.-X. Mao, H. Wang, Y.-G. Fu, B.F. Spencer Jr., Automated modal identification using principal component and cluster analysis: Application to a long-span cable-stayed bridge, Struct. Control Health Monit. 26 (10) (2019) e2430.
[18] G. Fan, J. Li, H. Hao, Improved automated operational modal identification of structures based on clustering, Struct. Control Health Monit. 26 (12) (2019) e2450.
[19] H. Mostafaei, M. Ghamami, P. Aghabozorgi, Modal identification of concrete arch dam by fully automated operational modal identification, Structures 32 (2021) 228–236.
[20] C. Rainieri, G. Fabbrocino, Development and validation of an automated operational modal analysis algorithm for vibration-based monitoring and tensile load estimation, Mech. Syst. Signal Process. 60 (2015) 512–534, http://dx.doi.org/10.1016/j.ymssp.2015.01.019, cited By 110.
[21] G. Quaranta, C. Demartino, Y. Xiao, Experimental dynamic characterization of a new composite glubam-steel truss structure, J. Build. Eng. 25 (2019) 100773.
[22] A. Aloisio, R. Alaggio, M. Fragiacomo, Dynamic identification and model updating of full-scale concrete box girders based on the experimental torsional response, Constr. Build. Mater. 264 (2020) 120146.
[23] R. Alaggio, A. Aloisio, E. Antonacci, R. Cirella, Two-years static and dynamic monitoring of the Santa Maria di Collemaggio basilica, Constr. Build. Mater. 268 (2021) 121069.
[24] A. Aloisio, M.M. Rosso, R. Alaggio, Experimental and analytical investigation into the effect of ballasted track on the dynamic response of railway bridges under moving loads, J. Bridge Eng. 27 (10) (2022) 04022085.
[25] C. Priori, M. De Angelis, R. Betti, On the selection of user-defined parameters in data-driven stochastic subspace identification, Mech. Syst. Signal Process. 100 (2018) 501–523.
[26] M. Civera, L. Sibille, L.Z. Fragonara, R. Ceravolo, A dbscan-based automated operational modal analysis algorithm for bridge monitoring, Measurement (2023) 112451.
[27] G. Zonno, R. Aguilar, R. Boroschek, P.B. Lourenço, Automated long-term dynamic monitoring using hierarchical clustering and adaptive modal tracking: validation and applications, J. Civ. Struct. Health Monit. 8 (2018) 791–808.
[28] E. Garcia-Macias, F. Ubertini, MOVA/MOSS: Two integrated software solutions for comprehensive structural health monitoring of structures, Mech. Syst. Signal Process. 143 (2020) http://dx.doi.org/10.1016/j.ymssp.2020.106830, cited By 35.
[29] P. Verboven, E. Parloo, P. Guillaume, M. Van Overmeire, Autonomous structural health monitoring—part I: modal parameter estimation and tracking, Mech. Syst. Signal Process. 16 (4) (2002) 637–657.
[30] M. Scionti, J. Lanslots, Stabilisation diagrams: Pole identification using fuzzy clustering techniques, Adv. Eng. Softw. 36 (11–12) (2005) 768–779, http://dx.doi.org/10.1016/j.advengsoft.2005.03.029, cited By 51.
[31] E. Neu, F. Janser, A. Khatibi, A. Orifici, Fully automated operational modal analysis using multi-stage clustering, Mech. Syst. Signal Process. 84 (2017) 308–323, http://dx.doi.org/10.1016/j.ymssp.2016.07.031, cited By 75.
[32] V. Mugnaini, L.Z. Fragonara, M. Civera, A machine learning approach for automatic operational modal analysis, Mech. Syst. Signal Process. 170 (2022) 108813.
[33] M.D.A. Hasan, Z. Ahmad, M.S. Leong, L. Hee, M.H.M. Idris, Cluster analysis for automated operational modal analysis: A review, in: MATEC Web of Conferences, Vol. 255, EDP Sciences, 2019, p. 02012.
[34] S. Chauhan, D. Tcherniak, Clustering approaches to automatic modal parameter estimation, in: Proceedings, International Modal Analysis Conference, IMAC, 2008.
[35] D. Liu, Y. Bao, H. Li, Machine learning-based stochastic subspace identification method for structural modal parameters, Eng. Struct. 274 (2023) 115178.
[36] G.C. Marano, M.M. Rosso, A. Aloisio, G. Cirrincione, Generative adversarial networks review in earthquake-related engineering fields, Bull. Earthq. Eng. (2023) 1–52.
[37] E. Reynders, R. Pintelon, G. De Roeck, Uncertainty bounds on modal parameters obtained from stochastic subspace identification, Mech. Syst. Signal Process. 22 (4) (2008) 948–969.
[38] R. Pintelon, P. Guillaume, J. Schoukens, Uncertainty calculation in (operational) modal analysis, Mech. Syst. Signal Process. 21 (6) (2007) 2359–2373, http://dx.doi.org/10.1016/j.ymssp.2006.11.007, cited By 153.
[39] E.P. Reynders, Uncertainty quantification in data-driven stochastic subspace identification, Mech. Syst. Signal Process. 151 (2021) 107338.
[40] C. Rainieri, G. Fabbrocino, Influence of model order and number of block rows on accuracy and precision of modal parameter estimates in stochastic subspace identification, Int. J. Lifecycle Perform. Eng. 1 (4) (2014) 317–334, cited By 34.
[41] K. Zhou, Q.-S. Li, X.-L. Han, Modal identification of civil structures via stochastic subspace algorithm with Monte Carlo–based stabilization diagram, J. Struct. Eng. 148 (6) (2022) 04022066.
[42] K. Zhou, Q.-S. Li, Modal identification of high-rise buildings under earthquake excitations via an improved subspace methodology, J. Build. Eng. 52 (2022) 104373.
[43] A.B. Owen, A randomized Halton algorithm in R, 2017, arXiv preprint arXiv:1706.02808.
[44] T. Hou, D. Nuyens, S. Roels, H. Janssen, Quasi-Monte Carlo based uncertainty analysis: Sampling efficiency and error estimation in engineering applications, Reliab. Eng. Syst. Saf. 191 (2019) 106549.
[45] E.N. Chatzi, M.D. Spiridonakos, A.W. Smyth, Implementation of parametric methods for the treatment of uncertainties in online identification, in: Identification Methods for Structural Health Monitoring, Springer, 2016, pp. 51–87.
[46] A. Gramacki, Nonparametric Kernel Density Estimation and Its Computational Aspects, Vol. 37, Springer, 2018.
[47] B.W. Silverman, Density Estimation for Statistics and Data Analysis, Routledge, 2018.
[48] C.M. Bishop, N.M. Nasrabadi, Pattern Recognition and Machine Learning, Vol. 4, No. 4, Springer, 2006.
[49] M.P. Wand, M.C. Jones, Kernel Smoothing, CRC Press, 1994.
[50] Z.I. Botev, J.F. Grotowski, D.P. Kroese, Kernel density estimation via diffusion, 2010.
[51] T. Odland, tommyod/KDEpy: Kernel Density Estimation in Python, Zenodo, 2018, http://dx.doi.org/10.5281/zenodo.2392268.
[52] A. Géron, Hands-on Machine Learning with Scikit-Learn, Keras, and TensorFlow, O'Reilly Media, Inc., 2022.
[53] S. Raschka, V. Mirjalili, Python Machine Learning: Machine Learning and Deep Learning with Python, Scikit-Learn, and TensorFlow 2, Packt Publishing Ltd, 2019.
[54] E.R. Ziegel, Methods of multivariate analysis, Technometrics 45 (1) (2003) 109.
[55] M.Y. Ata, A convergence criterion for the Monte Carlo estimates, Simul. Model. Pract. Theory 15 (3) (2007) 237–246.
[56] P.-H. Chan, J. Stebbins, A.B. Zavatsky, Efficacy of quantifying marker-cluster rigidity in a multi-segment foot model: a Monte-Carlo based global sensitivity analysis and regression model, Comput. Methods Biomech. Biomed. Eng. 25 (3) (2022) 308–319.
[57] L. Benedetti, F. Claeys, I. Nopens, P.A. Vanrolleghem, Assessing the convergence of LHS Monte Carlo simulations of wastewater treatment models, Water Sci. Technol. 63 (10) (2011) 2219–2224.
[58] M. Frigge, D.C. Hoaglin, B. Iglewicz, Some implementations of the boxplot, Amer. Statist. 43 (1) (1989) 50–54.
[59] H. Wickham, L. Stryjewski, 40 Years of boxplots, Amer. Statist. (2011) 2011.

[60] H. Sun, J. Al-Qazweeni, J. Parol, H. Kamal, Z. Chen, O. Büyüköztürk, Computational modeling of a unique tower in Kuwait for structural health monitoring: Numerical investigations, Struct. Control Health Monit. 26 (3) (2019) e2317.
[61] D. Parker, A. Wood, The Tall Buildings Reference Book, Routledge, 2013.
[62] C. Gu, G.A. Prieto, A. Al-Enezi, F. Al-Jeri, J. Al-Qazweeni, H. Kamal, S. Kuleli, A. Mordret, O. Büyüköztürk, M.N. Toksöz, Ground motion in Kuwait from regional and local earthquakes: Potential effects on tall buildings, Pure Appl. Geophys. 175 (2018) 4183–4195.
[63] P. Welch, The use of fast Fourier transform for the estimation of power spectra: a method based on time averaging over short, modified periodograms, IEEE Trans. Audio Electroacoust. 15 (2) (1967) 70–73.
[64] D.A. Dickey, W.A. Fuller, Distribution of the estimators for autoregressive time series with a unit root, J. Amer. Statist. Assoc. 74 (366a) (1979) 427–431.
[65] D.A. Dickey, W.A. Fuller, Likelihood ratio statistics for autoregressive time series with a unit root, Econometrica (1981) 1057–1072.
[66] B.J. O'Connell, T.J. Rogers, A robust probabilistic approach to stochastic subspace identification, 2023, arXiv preprint arXiv:2305.16836.
[67] M. Xu, F.T. Au, S. Wang, H. Tian, Operational modal analysis under harmonic excitation using Ramanujan subspace projection and stochastic subspace identification, J. Sound Vib. 545 (2023) 117436.
[68] F. Liu, J. Wu, F. Gu, A.D. Ball, et al., An introduction of a robust OMA method: CoS-SSI and its performance evaluation through the simulation and a case study, Shock Vib. 2019 (2019).